Evaluation and selection of biochars and hydrochars derived from agricultural wastes for the use as adsorbent and energy storage materials

J. Lang[1], L. Matějová[1], A.K. Cuentas-Gallegos[2], D.R. Lobato-Peralta[2], K. Ainassaari[3], M.M. Gómez[4], J.L Solís[4], D. Mondal[5], R. L. Keiski[3], G.J.F. Cruz[6*]

[1]Energy and Environmental Technology Centre, VSB - Technical University of Ostrava, 17. Listopadu 2172/15, 708 00 Ostrava-Poruba, Czech Republic

[2]Instituto de Energías Renovables, Universidad Nacional Autónoma de México, Priv. Xochicalco s/n, Col. Centro, Temixco, Morelos, CP 62580, México

[3]Environmental and Chemical Engineering, University of Oulu, P.O.Box 4300, FI-90014 University of Oulu, Finland

[4]Facultad de Ciencias, Universidad Nacional de Ingeniería, Av. Túpac Amaru 210, Lima 25, Perú

[5]Institute of Medical and Biomedical Education St George's, University of London, SW17 0RE, United Kingdom

[6]Departamento de Ingeniería Forestal y Gestión Ambiental, Facultad de Ciencias Agrarias, Universidad Nacional de Tumbes, Ciudad Universitario s/n Pampa Grande, Tumbes, Perú

*Corresponding author. Tel: +51 968 811 513. E-mail: gcruzc@untumbes.edu.pe (Gerardo J. F. Cruz)

Abstract

The utilization of unconventional agricultural wastes to obtain new porous carbonaceous materials, at mild pyrolysis temperatures and without complex procedures, for either water treatment and energy storage applications is important from the economic and environmental perspective. In this study, biochars and hydrochars were prepared from banana rachis, cocoa pod husks, and rice husks at 600 °C-2h, under nitrogen flux. The prepared materials were characterized to better understand how their morphological, textural, physical-chemical and/or structural properties correlate with their methylene blue (MB) adsorption capacities. The material with the best properties (mainly S_{BET}>800 m^2/g) and MB adsorption capacity was a novel biochar prepared from banana rachis (BW-BC). This novel material was selected for additional kinetics and equilibrium adsorption tests for lead (Pb) along with its energy storage capacity. In equilibrium test, the novel biochar reached a maximum adsorption capacity for methylene blue of 243.4 mg/g and the highest adsorption capacity for Pb(II) of 179.7 mg/g. In the kinetic adsorption test, the equilibrium adsorption value for methylene blue was 150.4 mg/g and that for Pb(II) was 159.6 mg/g. Most importantly, the performance of the BW-BC material for energy storage in supercapacitors surpassed that of the commercial activated carbon YP50F in neutral and acidic electrolytes, reaching specific energy values of 6.66 and 8.52 Wh/kg in acidic and basic electrolytes, respectively. Among the evaluated hydrochar and biochars derived of agrowastes, the biochar prepared from banana rachis showed the best properties, being potentially useful as adsorbent or as an electrode material for energy storage.

Keywords: biochar; hydrochar; banana rachis; lead; water treatment; supercapacitor

1. Introduction

Banana, cocoa and rice are three crops produced in tropical and subtropical areas, but with global importance. The three crops are important for food security worldwide and livelihood opportunities [1]. However, harvesting and handling of these crops generate various types of agricultural wastes, such as cocoa pod husks, banana rachis and pseudo-stems [2-6] as well as rice husks. A huge amount of these residues is either dumped or burned under open field conditions, which leads to pollution and affects the surrounding population. Unfortunately, only a little portion of the residues are used in animal feed or as construction materials in rural areas [7-9]. Since these materials are lignocellulosic in nature, they are potential raw materials for producing porous carbonaceous materials. These carbonaceous materials can be used in various fields, such as the food industry, water and wastewater treatment, renewable energy storage, carbon sequestration, and catalytic processes. [10, 11].

Currently, two of the most promising applications of carbonaceous materials are in water treatment and renewable energy storage. The carbonaceous material based adsorbents such as activated carbon, biochars and their composites are often used for water and soil treatment [12-15]. The adsorption process has been widely used in water treatment to remove various organic and inorganic contaminants from both wastewater and contaminated natural water. Methylene blue and lead are two pollutants widely studied due to human health and environmental concerns. Methylene blue belongs to the cationic dye family, which is used mainly in the textile industry and forms part of their effluents. This organic pollutant potentially affects the environment and can have detrimental effects on human health [16]. The effects on the environment include the disruption of the photosynthetic process in aquatic ecosystems. This dye is usually used as a model pollutant in different adsorption studies [16, 17].

By Contrast, lead is a heavy metal pollutant that is naturally present in a number of minerals such as (galena (PbS), cerussite ($PbCO_3$), and anglesite ($PbSO_4$). The lead pollution originates beside the natural occurrence from effluents from mining operations, metallurgy and it was formerly used in paints and in gasoline additives. It has a significant negative impact on human health that includes damages to the central nervous system, kidneys, liver, and reproductive system [18]. The toxic symptoms include anaemia, insomnia, headache, dizziness, and weakness of muscles. Lead is also considered a carcinogen [19].

Different renewable energy sources, such as wind power, are being used as an alternative for the production and consumption of highly polluting fossil fuels [20]. Due to the fluctuation in wind power production, the energy storage in this kind of systems is still a concern that must be addressed [20, 21]. Wind power energy production is more sustainable and environmentally friendly than fossil fuel energy production [22]. Supercapacitors are energy storage devices whose properties are between that of a conventional capacitor and a battery. Supercapacitors can store significantly more energy than traditional capacitors and have more power than batteries [23, 24]. Whereas a high-power battery requires 1 hour to discharge, a supercapacitor requires only a few seconds or minutes to do the same.

Carbonaceous materials are commonly used for both applications, however within this group, activated carbon is the most popular [25] based on its properties. Adsorption and storage energy performances of the carbonaceous materials depend, among other properties, on specific surface area, pore size distribution, surface chemistry, and structure. Biochars and hydrochars are part of a group of materials that are mostly obtained from lignocellulose feedstocks. Both materials require lower pyrolysis temperatures or fewer (or null) activation agents than activated carbons to be produced, representing a more feasible option from an environmental perspective. However, activated carbons usually present better properties than bare biochars and hydrochars. Properties of biochars and hydrochar could be improved via selection of adequate precursor (lignocellulosic biomass), manipulation of parameters during production process or modifications during production or post-production. These modifications include ultrasonication, metal impregnation, surfactant modification, microwave, electrochemical, plasma treatment techniques, among others [26]. Changes during or post- production process result in an increase of product cost and environmental concerns because of the use of chemicals or very high energy consumption and complexity. In the case of biochar, production at mild conditions ~600 °C under nitrogen flux has been used for different raw materials. However, in most cases, the obtained specific surface areas of the biochars were between 10-400 m^2/g; such as those derived of sunflower husk and rapeseed pomace (92.9-111.4 m^2/g)[27], banana pseudo-stem (133.25 m^2/g)[28], *Punica granatum* (195.32 m^2/g)[29], lotus seed pods (24.15 m^2/g)[30], sugar bagasse (388.3 m^2/g)[31], rice straw (10.3 -52.68 m^2/g)[32, 33], pomelo peel (27.5 m^2/g)[34], rice husk (377.1 m^2/g)[35]. Only a few of agricultural residues (not including wood) produced biochars with specific surface area higher than 500 m^2/g under those pyrolysis conditions. Materials, such as those derived of corn stover and cotton straw (500.8-527 m^2/g) [35, 36]. One alternative, from economic and environmental perspective, would be to find abundant and unconventional raw materials to produce biochars, at mild conditions.

Additionally, most of studies related to the production of hydrochar or biochar, derived of agricultural residues for adsorption or energy storage applications, analysed both applications from individual approach. A holistic environmental approach to simultaneously evaluate the produced material for both applications is of recent interest [37, 38]. This approach offers the possibility to find agricultural waste-based biochars with high added value.

In this study, two abundant (cocoa pod husk, and rice husk) and one unconventional (banana rachis) agricultural wastes were used for biochar and hydrochar production at mild conditions in one-step process. Based on their properties and methylene blue adsorption efficiency, the best material was selected for further evaluation for Pb(II) adsorption and energy storage applications. Banana rachis biochar is a novel porous material, produced at 600 °C-2 h under N_2 flux, with relevant specific surface area, comparable methylene blue and Pb(II) adsorption capacity and the potential to be used as a supercapacitor.

2. Materials and methods

2.1. Materials

The agricultural wastes, including banana rachis (BW), cocoa pod husk (CPH), and rice husk (RH), were collected from different production areas in the Tumbes region, northwestern Peru. The biomasses were washed with fresh water, dried at 80 °C until a constant weight was obtained, grounded and sieved to obtain a particle size of less than 0.5 mm.

During the adsorption experiments, methylene blue ($C_{16}H_{18}ClN_3S$) and lead chloride ($PbCl_2$) from Sigma Aldrich (reagents grade) were used for methylene blue (MB) and Pb solutions. Sulfuric acid (H_2SO_4), sodium sulphate (Na_2SO_4) and potassium hydroxide (KOH) provided by Merck were used as electrolytes in cyclic voltammetric experiments. During the electrode fabrication, carbon Super P (TIMCAL) and polytetrafluoroethylene suspension (Teflon, Sigma-Aldrich) were used.

2.2. Porous material production

The biochars were prepared by conventional pyrolysis under the following conditions. The biomass (50 g/batch) was heated to 600 °C at a heating rate of 10 °C/min (Tubular Furnace Naberthem GmbH, Germany, model R 120/500/12), in a flux of 150 mL/min nitrogen (technical grade, purity of 99.5 %) and controlled by a multi-gas controller Cole Parmer (USA) [16, 39]. Upon reaching 600 °C, the carbonization process was maintained for 2 h. Afterwards, the material was cooled to ambient temperature under a nitrogen atmosphere. The carbonized material was first washed with a 0.15 M HCl solution, and then washed 5 times with 500 mL of hot distilled water; it was finally washed with distilled water at room temperature until pH of the rinsed water was constant (~7). The dried and sieved materials (particle size less than 0.25 mm) were then assigned to the precursor material as “biochars” (–BC). The hydrochars (–HC) were prepared in an in-house carbonization setup with 1.2 L capacity (Figure S1) at 200 °C for 2 h under a pressure of 40 bars, using a water/material ratio of 10/1. The carbonized material was washed with HCl and then with hot distilled water; it was then washed with distilled water at room temperature and dried in the same manner as the biochars. The hydrochars were sieved to obtained particle size less than 0.25 mm.

2.3. Adsorbents characterization

To characterize the synthesized porous materials, their structure and phase compositions were analyzed using X-ray powder diffraction method in a Siemens D5000 diffractometer operated at 30 kV and 20 mA, CuKα (λ=1.5406 Å) radiation. The structure was also analyzed using a Raman spectroscopy, a Horiba (Japan) Jobin-Yvon LabRAM HR800 high-resolution confocal μ-Raman system with solid-state laser (638 nm) excitation. Nitrogen physisorption measurements were performed to determine textural properties of the produced hydrochars and biochars, using an ASAP2020 sorption set-up (Micromeritics, USA). The specific surface area, S_{BET}, was calculated from the adsorption branch of the nitrogen adsorption-desorption isotherm according to the classical Brunauer–Emmett–Teller (BET) theory for p/p_0 = 0.05-0.20 [40]. Since the specific surface area, S_{BET}, is not an accurate parameter for microporous-mesoporous solids [41], the mesopore surface area, S_{meso}, and the micropore volume, V_{micro}, were also evaluated based on the t-plot method using the Broekhoff-de Boer standard isotherm for accuracy [42]. The net pore volume, V_{net}, was determined from the nitrogen adsorption isotherm at maximum p/p_0 ~0.990. The mesopore-size distribution was calculate based on the adsorption branch of the nitrogen adsorption-desorption isotherm by the Barrett–Joyner–Halenda (BJH) method via the Roberts algorithm [43, 44], using the Broekhoff-de Boer standard isotherm with Faas correction and the assumption of the cylindrical-pore geometry (characterized by the diameter d_p of the pores). The morphology was studied using a field emission scanning electron microscope ULTRA PLUS FESEM (Zeiss, Germany). The materials were covered with a conductive coat of platinum before imaging. Energy dispersive spectrometry (EDS) analyses were carried out with a Bruker Oxford coupled to the FESEM equipment; however, the samples were not coated with platinum. FTIR analysis was conducted by FTIR spectrometer – Shimadzu Tracer-100 to detect functional groups present on the produced material surface within the wavenumber range of 4000–400 cm^{-1}. The equipment was equipped with an attenuated total reflectance (ATR) device.

For the material with the best textural properties and MB adsorption capacity, was determined pH at the point of zero charge (pH_{PZC}). The pH_{PZC} was calculated using the drift method [7].

2.4. Adsorption tests

In the equilibrium and kinetic adsorption tests, MB and Pb(II) were used as model organic and inorganic pollutants, respectively. Since MB is a good model pollutant, it is widely used and can be considered as a benchmark in the literature. In addition, the molecular size of MB is well known; therefore, the relationship between its kinetic adsorption results, pore size distribution, and molecular size of the adsorbent can be determined. Pb(II) was chosen because it is a hazardous compound found in rivers in Peru.

During the MB kinetic adsorption tests, 0.4 g (2 g/L) of biochar was added to a 200 mL of MB solution with a concentration of 250 mg/L in a flask. The mixture in the flask was stirred using an electromagnetic stirrer and aliquots were taken at the beginning and 2, 5, 10, 15, 20, 30, 60, 90, 120, 180 and 240 min. Regarding the hydrochars, the adsorbent load was 0.5 g (2.5 g/L) and the initial concentration of methylene blue was 50 mg/L (200 mL). The rest of the procedure was similar to that for biochars. Every aliquot that was taken during the kinetic experiments were filtered through a 0.45 μm syringe filter. To avoid the effect of syringe filter, the first 1 mL of filtered solution was discarded and then the rest of the sample was taken for analyses. The concentration of MB in the solution was determined using a UV-VIS spectrometer (UV-2600 Shimadzu) at 660 nm wavelength.

In the MB equilibrium adsorption tests conducted with biochars, 0.2 g (4 g/L) of biochar samples were added to 50 mL of each MB solution with initial concentrations of 50, 80, 100, 150, 200, and 250 mg/L. Regarding the banana rachis biochar (BW-BC), the adsorption isotherm collected with initial biochar load of 0.2 g was incomplete, therefore, the biochar load for this sample was readjusted to 0.02 g. In the equilibrium tests with MB adsorption of hydrochars, the initial adsorbent load was the same (4 g/L), but the initial concentrations of the MB were 5, 10, 20, 50, 80, 100 and 150 mg/L. This modified range of concentrations was satisfactory for achieving complete adsorption isotherms. The equilibrium adsorption tests lasted for 48 h in an orbital shaker incubator (Heidolph Unimax 1010) and the temperature was maintained at 30 °C throughout the period. The 48 h period was used for the equilibrium tests based on preliminary experiments with the same materials. At the end of the contact time, 10 mL aliquots were taken from each flask and filtered. From the filtered aliquots, 2 mL of solution was pipetted and diluted with distilled water in a 25 mL volumetric flask. The concentration of MB in each aliquot was determined using a UV-VIS spectrometer UV-2600 Shimadzu at 660 nm wavelength.

Based on the adsorbents properties and the results of MB adsorption experiments, the best adsorbent material was selected for further Pb(II) adsorption experiments. During Pb(II) experiments, 150 mL of Pb(II) solution with an initial concentration of 50 mg/L (Initial pH=6.5) and adsorbent loads of 0.3 g/L and 0.5 g/L were used. Aliquots were taken at the start and 2, 5, 10, 15, 20, 30, 60, 90, 120,180, and 240 min. Every aliquot (~10 ml) was preserved by adding 50 μl of concentrated nitric acid. The samples were kept in refrigeration conditions until Pb analysis were conducted using a high-resolution continuum source atomic absorption spectrometer (HR-CS-AAS) (Analytik Jena ContrAA 800D). In the equilibrium tests, the volume of each solution was 100 mL, the initial Pb(II) concentrations were 10, 20, 50, 80, 120 and 150 mg/L (initial pH = 6.5) and

0.5 g/L of the biochar was added. The experimental lasted for 48 h and the temperature was maintained at 30 °C. Aliquots were preserved with concentrated nitric acid and stored under refrigeration conditions until Pb analyses were performed.

Different non-linear models were applied to assess the experimental data obtained. During the kinetic tests, the pseudo-first and pseudo-second-order rate equations and the Elovich model were applied to fit the results. The intraparticle model was used to study the adsorbent transport mechanism. Langmuir, Freundlich and Dubinin-Radushkevich models were used for the equilibrium tests. The model equations and parameters are listed in Table S2. The application and evaluation of the models in their non-linear forms were performed using the Origin 2019b software.

2.5. Electrochemical characterization

Viability as an electrode material for energy storage devices was investigated for materials that showed the best textural properties in terms of their specific surface areas and surface functional groups. This selection was based on the results of our previous studies [45-48] since, materials with specific surface areas higher than 600 m^2/g displayed good electrochemical properties. The biochar powder (particle size less than 0.25 mm) was processed to form self-standing 1 cm^2 films. A paste of the electrode material was obtained using 60 % of biochar, 30 % of carbon black (Super P Li), and 10 % polytetrafluoroethylene (Sigma-Aldrich) as a binder. All components were mixed with ethanol (96 % V/V) at 60 °C until a black dough was obtained; then it was deposited in a stainless-steel mesh current collector and finally pressed for 2 min at 7 ton.

The electrochemical characterization was performed using a 3-electrode cell, employing the biochar as the working electrode, a graphite rod as the counter electrode, and SSE electrode as the reference. Three different aqueous electrolytes were tested: 0.5 M H_2SO_4, 1 M Na_2SO_4, and 1 M KOH as the acidic, neutral, and alkaline electrolytes, respectively. Potential window, i.e., the electric potential range where electrodes can work without decomposition, was determined for all the electrolytes by cyclic voltammetry (CV) at 20 mV/s. CV is an electrochemical technique aids in determining the electrochemical performance of a tested material and its viability as a supercapacitor electrode. The measurements were performed using a Biologic VMP-300 potentiostat controlled by an EC-Lab® software. Two-electrode supercapacitor cells were assembled using the electrolyte whose working electrodes had the best electrochemical behavior. Supercapacitor cells were assembled using an active area of 4 cm^2 instead of 1 cm^2 to make the cells more similar to a commercial supercapacitor. The following mathematical expression was used to determine the mass ratio for the asymmetric devices[49]:

$$\frac{m^+}{m^-} = \frac{C^- \cdot \Delta E^-}{C^+ \cdot \Delta E^+} \tag{1}$$

where m^+ and m^- (g) represent the active mass of a positive or negative electrode; C^+ and C^- are their capacitances (F/g), and ΔE^+ and ΔE^- (V) are the potential differences in the open circuit potential to the positive and negative limits of the potential window.

Galvanostatic charge/discharge cycling technique was used to evaluate the supercapacitors, using specific currents of 0.25, 0.50, 1.00, 1.50 and 2.00 A/g. In this technique a constant specific current is used to charge the device based on the potential windows determined in the 3-electrode cells. After charging, a current of the same intensity but with opposite polarity is employed to discharge the devices. Through this technique, it is possible to determine the amount of energy that the devices can store and their power. The efficiency of the supercapacitor can be determined using the same process. The capacitance, specific energy, and power were calculated using equations (2), (3) and (4) [46, 49].

$$C = \frac{I \cdot t}{V} \tag{2}$$

where C is the 2-electrode system capacitance (F/g); I is the applied current (A/g); t is the discharge time (s), and V the cell voltage (V).

$$E = \frac{\frac{1}{2} C \cdot V^2}{3600} \tag{3}$$

where E is the specific energy (Wh/kg); C is the capacitance (F/g); and V the cell voltage (V).

$$P = \frac{3600E}{t} \tag{4}$$

where P is the specific power (W/h); E is the specific energy (Wh/kg); and t is the discharge time (s).

In addition, The Coulombic and energy efficiencies were determined using equations (5) and (6), respectively [50].

$$\eta_{Coulombic} = \frac{t_d}{t_c} \tag{5}$$

where $\eta_{Coulombic}$ is the Coulombic efficiency t_d is the discharge time (s), and t_c is the charge time (s).

$$\eta_{Energy} = \frac{E_d}{E_c} \tag{6}$$

where η_{Energy} represents the energy efficiency, E_d is the energy delivered by the supercapacitor during discharge (J), and E_c is the energy received during the charge (J). Finally, electrochemical impedance spectroscopy (EIS) was used as an alternative current-based technique to complete the characterization of the supercapacitors (in terms of their resistances under optimum operational conditions). EIS was employed by applying potential oscillations of ±10 mV in the frequency range of 50 kHz to 5 mHz.

3. Results and discussion

3.1. Biochars and hydrochars characterization

3.1.1 Structural and textural characterization

Figure 1a depicts the X-ray diffractograms of the biochars, two large peaks were identified at 24° and 42°. These peaks correspond to the semi-amorphous phase which is typical of disordered carbonaceous materials, such as biochars [7]. Figure 1b shows the peaks in the diffractogram of hydrochars at 15.9°, 22.9° and 34.9°, which correspond to that of cellulose crystals, planes 110, 200 [51] and 040 [52], respectively. The cellulose is decomposed to amorphous or volatile aromatic carbon structures at high temperature [53, 54]; hence, they are missing in the case of biochars. Moreover, regarding the hydrochars, the hydrothermal conditions used could not decompose the cellulose of the precursors.

Figure 1c and 1d present the first order Raman spectra observed in biochars and hydrochars, respectively. As shown in Table S1, the Raman spectra are typical of carbonaceous materials (presence of D-and G-bands) [55] and were de-convoluted with a 5-band deconvolution model (G, D1, D2, D3, and D4) [56] (see Figure S2). The G-band “graphite” was caused by graphite lattice vibration mode with E2g symmetry [56, 57]. D-band (disorder band D1, D2, D3, D4) was caused by disorders (defects and in the proximity of edges) in the graphene lattice [58, 59]. The I_{D1}/I_G band intensity gives information about the graphitization degree (decreasing of the I_{D1}/I_G indicates the formation of graphitic structure) [56], and as shown in the supporting material (Table S1), there are not differences in graphitization among the materials. The spectra of BW-HC indicate strong fluorescence of the material at excitation λ_{exc} = 638 nm and does not provide any useful signal. However, the spectra of RH-HC indicated the presence of a shoulder at around 1086 cm^{-1} and 1422 cm^{-1}, which correspond to D bands, indicating a more disordered graphene lattice than in the rest of the materials.

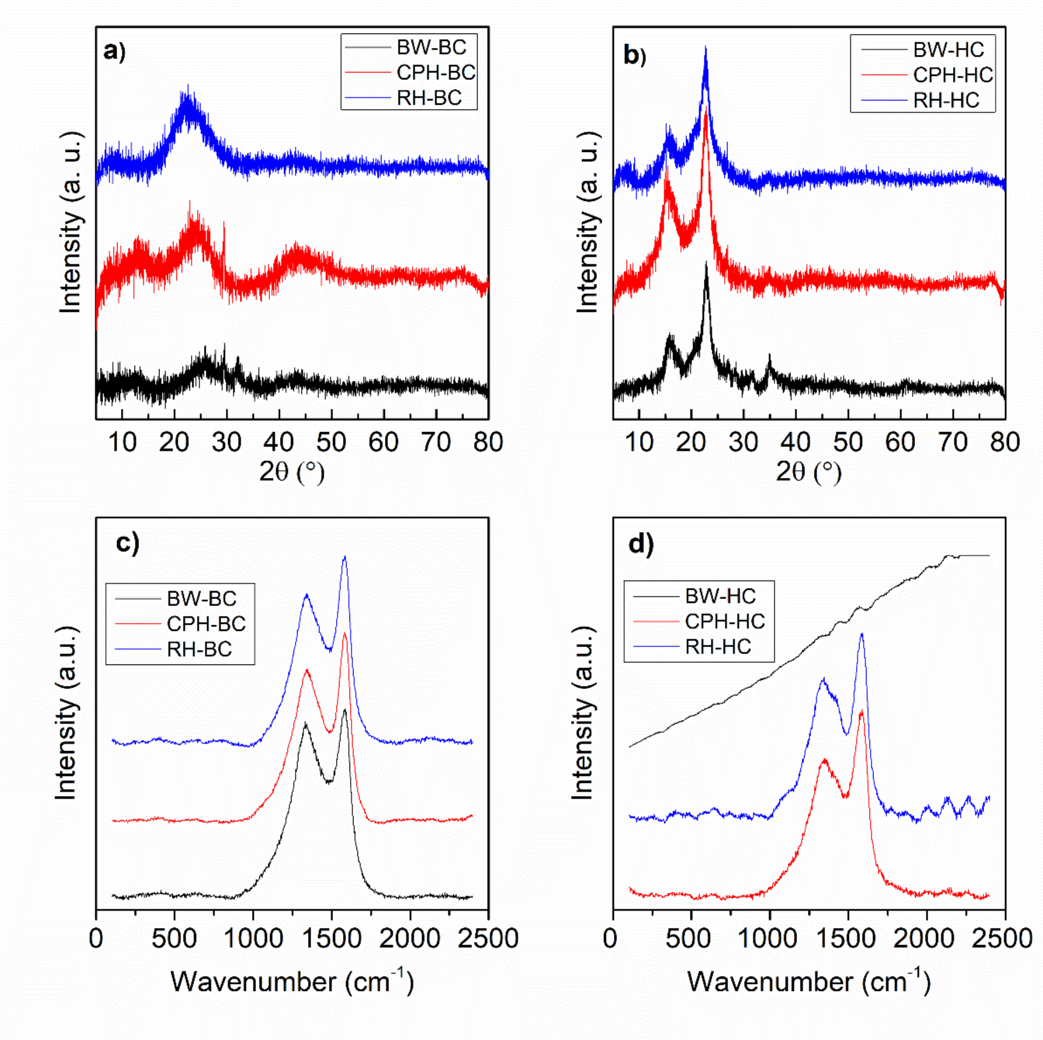

Figure 1. (a) and (b) depict the XRD diffractograms of biochars and hydrochars, respectively, whereas (c) and (d) depict the Raman spectra for the biochars and hydrochars, respectively.

When the measured adsorption-desorption isotherms from nitrogen physisorption measurements for both sets of materials are compared (Figure 2 a and c), i.e., biochars *versus* hydrochars, it is evident that the conventional pyrolysis of the selected agricultural wastes results in porous materials with well-developed microporous-mesoporous structure than by hydrothermal treatment. According to the IUPAC classification, hydrochars are mesoporous-macroporous solids characterized by type II isotherm (Figure 2c) [60] with a hysteresis loop at higher relative pressure range (mostly $p/p_0 \sim 0.7\text{-}0.99$). These features correspond to a generally low surface area (~7-17 m^2/g) and low total pore volume (0.031-0.070 cm_{liq}^3/g) of hydrochars. In contrast, biochars belong to microporous-mesoporous solids. All the biochars showed an increased nitrogen uptake at low p/p_0 (< 0.05), which is typical of type I isotherm related to microporous materials (Figure 2a) [60], and a hysteresis loop within the broad range of p/p_0 (0.2 or 0.4-0.99) correspond to that of well-developed mesopores.

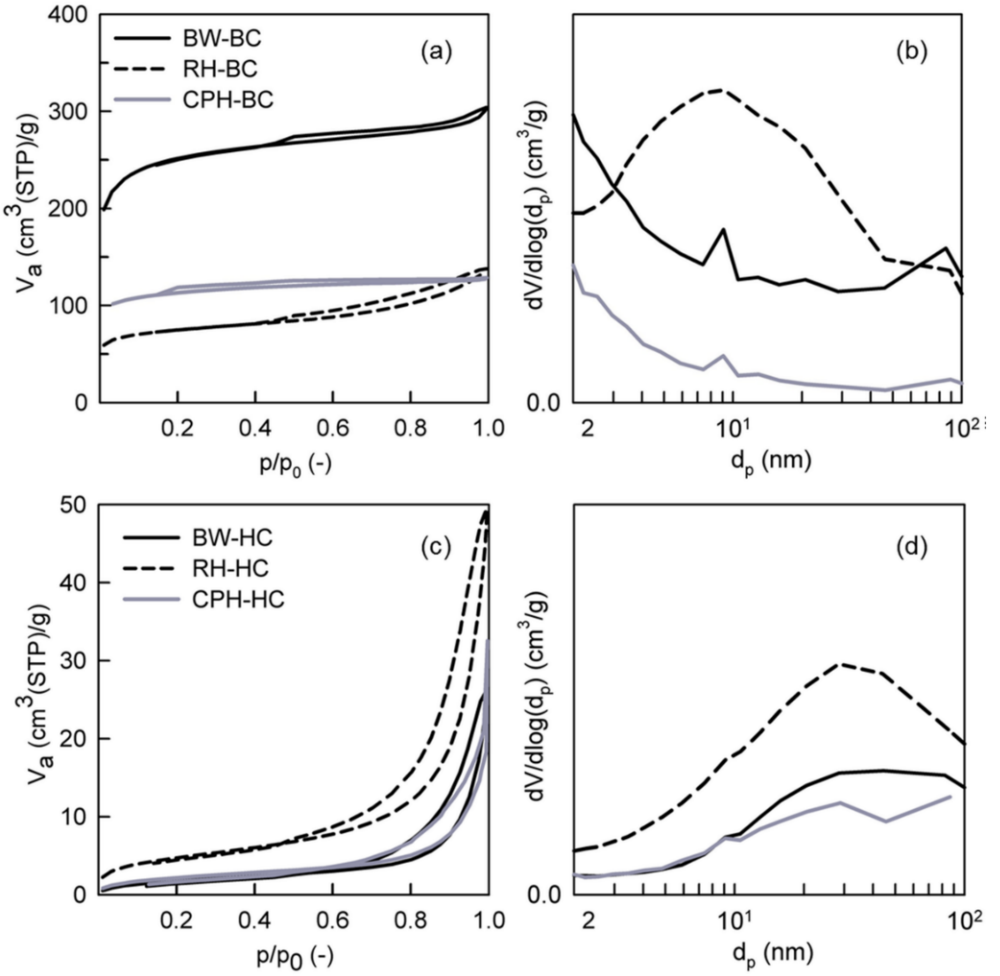

Figure 2. (a) and (c) are nitrogen adsorption-desorption isotherms, respectively, and (b) and (d) are evaluated pore-size distributions of biochars and hydrochars, respectively.

Table 1. Textural properties of the materials produced.

Property	**Biochar**			**Hydrochar**		
	BW-BC	**CPH-BC**	**RH-BC**	**BW-HC**	**CPH-HC**	**RH-HC**
S_{BET} (m^2/g)	859	383	256	7	8	17
S_{meso} (m^2/g)	276	113	103	7	8	17
V_{micro} (cm$_{liq}^3$/g)	0.265	0.124	0.069	0	0	0
V_{net} (cm$_{liq}^3$/g)	0.470	0.196	0.210	0.040	0.031	0.070

Consequently, biochars possess a high volume of micropores (0.069-0.265 cm$_{liq}^3$/g), larger mesopore surface areas (103-276 m^2/g), and higher total pore volumes (0.196-

0.470 cm_{liq}^3/g) (Table 1). The differences in the textural properties *(i.e.* in specific surface area, net pore volume etc.) in the frame of biochars/hydrochars may be due to the different organic composition, such as lignin, cellulose, and hemicellulose contents [61], of individual agricultural waste (BW *vs.* CPH *vs.* RH). Previous studies on the lignocellulosic content of the three precursors used in this study found different compositions. BW contains 35.3 % of cellulose, 17.9 % of hemicellulose, and 6 % of lignin [62]; CPH contains 19.7 – 26.1 % of cellulose, 8.7 – 12.8 % of hemicellulose, and 14 – 28 % of lignin [2]; and RH contains 62.2 % of cellulose + hemicellulose, and 21.8 % of lignin [63].

Compared with that of hydrochars, the significantly improved porosity of biochars might be due to the treatment conditions the agricultural wastes were subjected to—conventional pyrolysis done in a gas phase at elevated temperature of 600 °C for 2 h versus hydrothermal treatment done in a liquid phase under elevated pressure of 40 bars and temperature of 200 °C for 2 h. It seems that the degradation/dissolution of organic compounds and the heat and mass transferred during the conventional pyrolysis surpassed the conditions set for the hydrothermal treatment, making the conventional pyrolysis more effective.

Biochar derived from banana rachis, was from all the tested materials, the material with the best textural properties, including specific surface area, pore volume and meso-microporous structure. The specific surface area (859 m^2/g) was higher than those of biochars made of other agricultural residues produced under similar conditions (between 10 – 530 m^2/g according to the literature survey showed in the introduction). Banana rachis is a novel raw material with the potential to produce biochars with promising textural properties.

3.1.2. Morphological, surface functional groups and elemental characterization

FESEM images of the produced materials are shown in Figure 3. In the case of biochar and hydrochar made from banana rachis (BW) (Figures 3a and b, respectively) and cocoa pod husk (CPH) (Figure 3c and d, respectively), their morphologies are different. It is possible to identify a porous structure in both biochars, whereas in the case of both hydrochars, a more rugged morphology without defined porosity is observed. The morphologies of biochar and hydrochar made of rice husk (RH) (Figures 3e and 3f, respectively) are similar to long channels. The pores of biochar derived from rice husk are identified inside the channels.

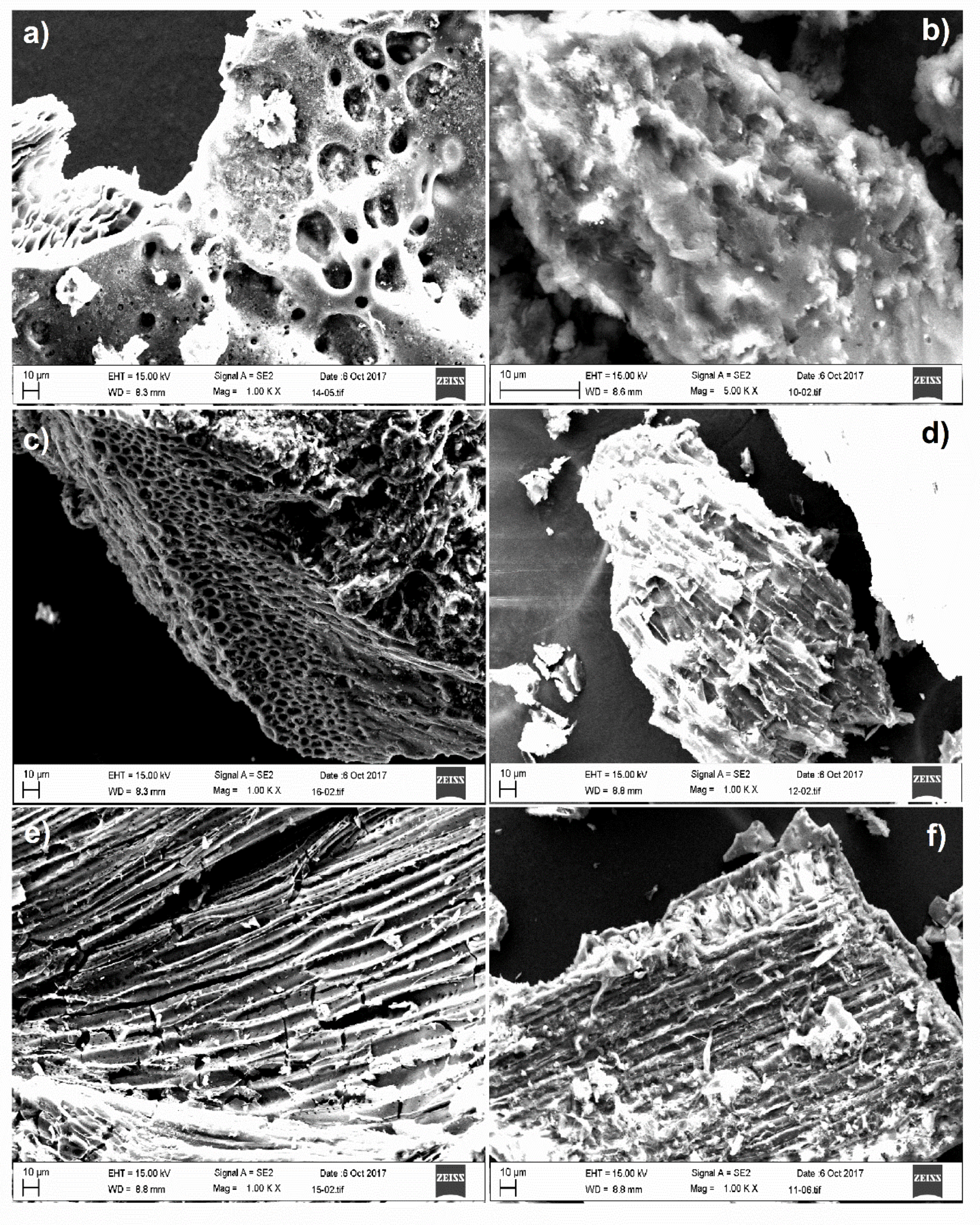

Figure 3. FESEM pictures of the produced biochars and hydrochars, a) BW-BC, b) BW-HC, c) CPH-BC, d) CPH-HC, e) RH-BC, and f) RH-HC.

The average surface chemical composition (%wt) of the adsorbents determined by EDS analysis is depicted in Table S3. All adsorbents are composed mostly of C and O. Biochars contain between 62.6 – 75.9 %(wt) and 18.6 – 24.7 %(wt) of C and O, respectively; whereas hydrochars contain between 46.1 – 70.1 %(wt) and 29.0 – 35.7 %(wt) of C and O, respectively. The remaining elements are major or minor elements that are usually present in this type of products [64]. Ca is present in high level in BW-BC and CPH-BC; whereas Si is present in high levels in BW-BC, RH-BC, BW-HC and much more in RH-HC (18.1 %wt). RH-HC shows a very heterogeneous structure with high standard deviations (see C and Si content in Table S3). Other elements present in the material include K, Mg, Cu, P, Al, Fe, and S.

The ATR-FTIR analysis (Figure S3) confirmed the presence of different functional groups in the samples of biochar and hydrochar. Biochars showed a common peak at 2346 cm^{-1}, which corresponds to C=O of ketone group [65]. Spectra of BW-BC and CPH-BC present a peak at 1531 cm^{-1}, which corresponds to carboxyl groups (-COOH) or C=C stretching vibrations [66, 67]. Additionally, BW-BC spectrum shows peaks at 1209 and 1007 cm^{-1}, which correspond to -C-O ether alcohol and ether group [68, 69]. CPH-BC spectrum shows an additional peak at 1391 cm^{-1}, which corresponds to ether groups R-O-R’, (1376 cm^{-1}). Additional peak at 1601 cm^{-1}, in the RH-BC spectrum, corresponds to C=O in aromatics and C=O or C=C [69, 70]. Peaks at 1079 and 457 cm^{-1} in RH-BC spectra could correspond to Si-O-Si [71]. Si content, found by EDS in the RH-BC, is in agreement with this finding.

Hydrochars spectra present a common peak at 1602-1603 cm^{-1}, which corresponds to C=O or C=C groups vibrations [72, 73]. BW-HC and CPH-HC spectra present additional peaks at 2346-2347 cm^{-1} and 1429-1434 cm^{-1}, which correspond to C=O [65] and C-H bending and stretching [74]. The peak at 1064 cm^{-1} in the sample CPH-HC corresponds to C-O-C [75]. However, in the case of BW-HC and RH-HC, the peaks at 1013-1037 and 446-445 cm^{-1} could correspond to Si-O-Si [71, 76].

3.2. Methylene blue adsorption tests

Figures 4a and c show the results of MB kinetic experiments of biochar and hydrochars, respectively. Among the biochars, BW-BC has a significantly better adsorption capacity than CPH-BC and RH-BC. BW-BC reached equilibrium in the first 50 min of the experiments, whereas CPH-BC and RH-BC reached equilibrium in the first 90 to 120 min. The better adsorption capacity of BW-BC might be because of its better textural properties, which are higher specific surface area, mesoporous area, and microporous volume. Since BW-BC is a microporous-mesoporous material, it is able to adsorb MB at a very high initial rate and can adsorb more amounts of MB in the equilibrium stage. In aqueous systems, size exclusion limit is observed when the pore width is smaller than about 1.7 times the second largest dimension of the adsorbate [77-79]. MB had a molecular size of 1.66×0.82×0.54 nm [16] and size exclusion limit of 1.4 nm. Regarding pore size distribution (PSD) (Figure 2b), BW-BC showed pores in all the analyzed range of pore width between 0 to 100 nm, with a tendency to increase the number of pores in the range of 10 to 0 nm. Regarding the size exclusion limit of MB and the PSD of BW-BC, the adsorption is effective; however, it is limited to the microporous region between 0 and 1.4 nm of pore width.

Regarding the hydrochars (Figure 4c), BW-HC and RH-HC started to reach equilibrium after 240 min of the kinetic experiment. CPH-HC did not reach equilibrium in this period (240 min). All hydrochars revealed a mesoporous-macroporous structure with almost null microporosity. RH-HC showed higher specific surface area than BW-HC and CPH-HC, but it showed the lowest adsorption capacity. A possible reason for the low adsorption capacity of RH-HC is due to its lack of surface functional groups (2346-2347 cm^{-1} and 1429-1434 cm^{-1}, which correspond to C=O and C-H bending and stretching) and presence of impurities, such as Si, on its surface, according to the table S3 (EDS analyses). The presence of Si as impurity on the surface could have affected the adsorption phenomena by blocking the active sites on the adsorbent surface.

The kinetic data of MB adsorption of BW-BC fit best to the pseudo-second-order model, whereas the kinetic data of CPH-BC and RH-BC fit best to the Elovich model (Table 2). Regarding the hydrochars, the kinetic data of BW-HC fit best to the first-order kinetic model, and the two other sample data fit best to the Elovich model.

The intraparticle diffusion model (Figures 4e and f and Table 2) was applied to the kinetic data. In Table 2, the parameters marked 1, 2, and 3 correspond to the surface diffusion, intraparticle diffusion, and equilibrium adsorption to the surface, respectively. Regarding the BW-BC, CPH-BC, and RH-BC biochars (Figure 4 e), 3 stages of the adsorption phenomena were identified, which suggests that intraparticle diffusion could be one of the rate-limiting mechanisms. The rate of adsorption in the 3 stages (k_{Diff1}, k_{Diff2}, and k_{Diff3}) reduces with every stage, i.e., $k_{Diff1} > k_{Diff2} > k_{Diff3}$. The adsorption rate in the surface diffusion stage is higher due to the presence of available adsorption active sites since intraparticle diffusion is limited by the accessibility of pores and the molecular size of MB. Finally, the equilibrium stage occurs at a lower rate since the adsorbate has to occupy the active sites in the micropores (inner part of the adsorbent).

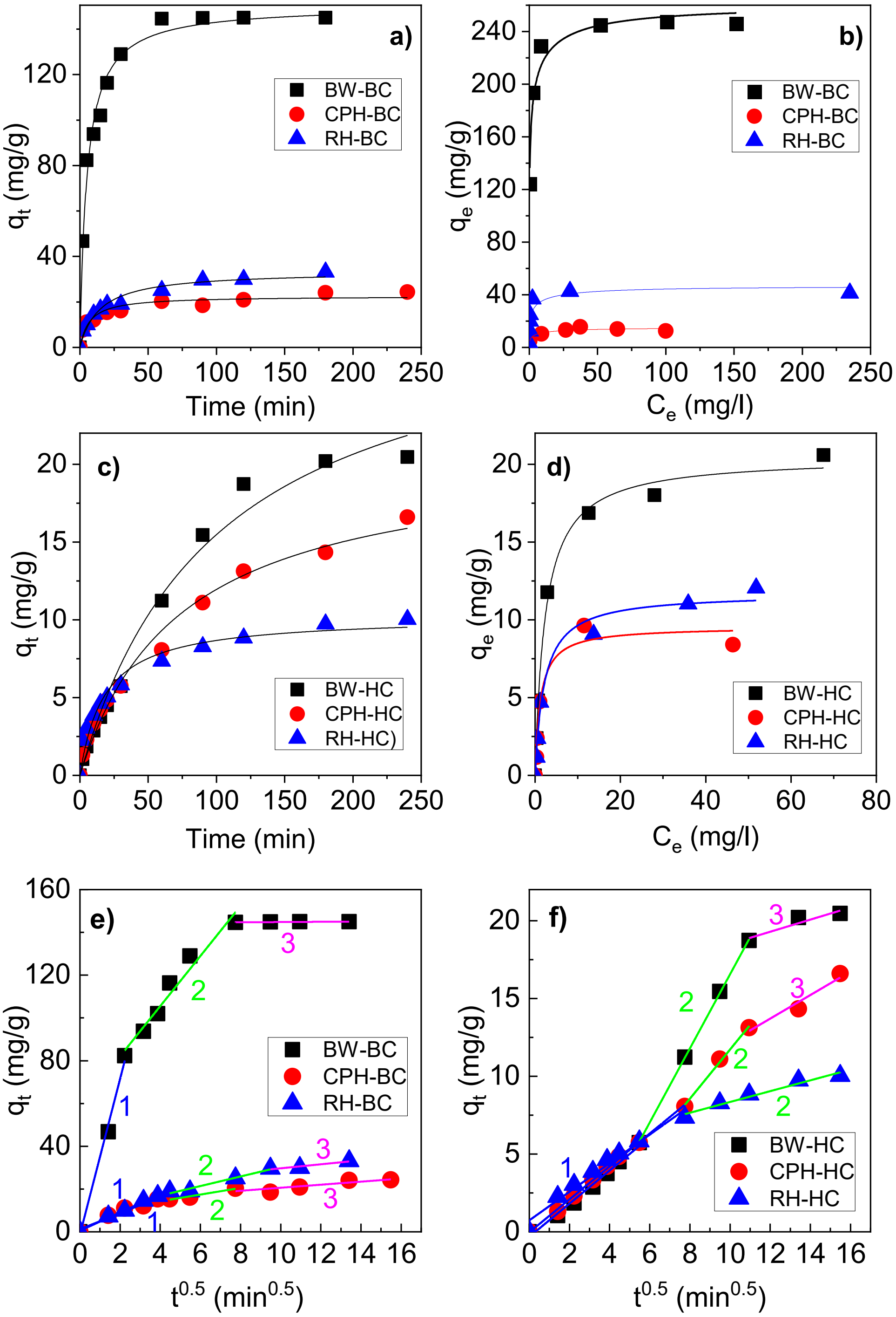

Figure 4. (a) and (c) show the methylene blue kinetic adsorption results, respectively; (b) and (d) show the methylene blue equilibrium isotherms, respectively, and (e) and (f) show the application of intraparticle diffusion model to the kinetic adsorption data for biochars and hydrochars, respectively.

Table 2. Parameters of the models applied to results of the kinetic test with methylene blue.

Model	Parameter	Biochar			Hydrochar		
		BW-BC	CPH-BC	RH-BC	BW-HC	CPH-HC	RH-HC
Pseudo-first order	q_1(mg/g)	139.5	20.8	29.5	22.4	16.1	9.0
	K_1(min^{-1})	0.123	0.094	0.054	0.012	0.014	0.044
	R^2	0.948	0.865	0.928	0.992	0.974	0.929
	X^2	128.223	7.345	8.632	0.525	0.859	0.790
Pseudo-second order	q_e (mg/g)	150.4	22.6	33.5	30.9	20.7	10.2
	K_2(g/mg.min)	0.001	0.006	0.002	3.2×10^{-4}	6.5×10^{-4}	0.005
	R^2	0.988	0.936	0.968	0.987	0.984	0.969
	X^2	30.717	3.506	3.779	0.899	0.540	0.343
Elovich	*a (mg/g.min)*	146.6	14.1	4.9	0.4	0.4	1.3
	b (mg/g)	0.045	0.288	0.149	0.101	0.172	0.503
	R^2	0.971	0.983	0.992	0.980	0.991	0.995
	X^2	72.208	0.954	0.913	1.354	0.316	0.057
Intraparticle diffusion	k_{Diff1} *(mg/g.min*$^{-0.5}$*)*	36.389	3.777	4.243	1.065	1.058	0.919
	C_1 *(mg/g)*	~0	1.173	0.554	-0.318	-0.027	0.738
	R_1^2	0.995	0.955	0.994	0.989	0.998	0.969
	k_{Diff2} *(mg/g.min*$^{-0.5}$*)*	11.714	1.557	2.239	2.381	1.581	0.348
	C_2 *(mg/g)*	58.670	8.073	7.959	-7.257	-4.092	4.871
	R_2^2	0.962	0.974	0.965	1.000	0.995	0.962
	k_{Diff3} *(mg/g.min*$^{-0.5}$*)*	0.059	0.712	0.937	0.390	0.758	-(*)
	C_3 *(mg/g)*	144.243	13.480	20.325	14.607	4.616	-
	R_3^2	0.686	0.768	0.923	0.896	0.950	-

(*) Data is not showed because the third stage is missing in this sample

The BW-HC and CPH-HC hydrochars showed three defined sections in the curve $t^{0.5}$ and q_t (Figure 4f); however, the adsorption equilibrium stage was not reached. The rate of the second region of the curve (k_{Diff2} in Table 2) was higher than the rate of the first region (k_{Diff1}); this is the opposite of what happens when the data fit the multistep diffusion model. Regarding RH-HC, its respective curves $t^{0.5}$ and q_t (Figure 4f) could only be divided into two sections. Therefore, compared with the molecular size of the MB, since the textural structure of the material is poor and the values are negative (C_1, C_2, and C_3), the multistep approach of intraparticle diffusion is not the rate-limiting mechanism. The obtained hydrochars were mainly mesoporous-macroporous. Based on the molecular size of MB, it is expected that the diffusion mechanism would not be the rate-limiting adsorption mechanism for hydrochars.

The biochar and hydrochar isotherms from the equilibrium adsorption tests with MB are shown in Figures 4b and 4d, respectively. Based on the scale of the y-axis of both figures (0–250 mg/g and 0–25 mg/g for biochars and hydrochars, respectively), it is possible to corroborate that the obtained biochars are better materials to adsorb MB. BW-BC was the best adsorbent material, adsorbing high amounts of MB with small adsorbent loading.

Most of the equilibrium adsorption data fit best to the Langmuir model with R^2 between 0.801–0.994. Only CPH-BC and RH-HC samples fit the Dubinin-Raduskevich model, with R^2 between 0.865–0989. In the Langmuir model, the separation factor R_L was found to be <1 (the isotherm curve is favourable) for all the tested materials. The maximum adsorption capacities in equilibrium calculated from the best model to fit (Langmuir or Dubinin-Radushkevich) are shown in Table 3. They were 243.4 mg/g for BW-BC, 15.1 mg/g for CPH-BC, 43.2 mg/g for RH-BC, 20.4 mg/g for BW-HC, 9.5 mg/g for CPH-HC, and 13.9 mg/g for RH-HC. BW-BC demonstrated the highest overall Q_{max} because of its large specific surface area and distribution of pores, and it is suitable for adsorbing the pollutants of the chosen model.

The magnitude of adsorption energy E (kJ/mol) determined from the Dubinin-Raduskevic model can provide useful information about the type of adsorption process that takes place, whether physical (E<8 kJ/mol), ion exchange (E= 8-16 kJ/mol), or chemical (E>16kJ/mol) [80]. As shown in table 3, the energies E determined for adsorption of MB were all within 8-16 kJ/mol. This means that the MB adsorption process of the biochar and hydrochar is due to ion exchange. Different functional groups present on the materials surface of biochar and hydrochars, detected by FTIR, could be responsible for the electron exchange with MB molecules.

Regarding the biochars, the rate-limiting mechanisms depend on multistep intraparticle diffusion and ion exchange. Hydrochar adsorption mechanism of methylene blue mainly depends on ion exchange.

BW-BC was the material with the best MB maximum adsorption capacity, which is comparable with that of biochars prepared from different lignocellulosic biomasses. The MB maximum adsorption capacity of BW-BC is 243.4 mg/g, whereas for biochars produced from mentha plant waste is 86-588 mg/g [81], from seaweed is 512 mg/g [82], from banana peel is 390 mg/g [83], from *Wodyetia bifurcate* is 149 mg/g [84], from leaf of *Magnolia grandiflora* is 101 mg/g [85], and from oak wood is 98 mg/g [86]. Further comparisons and conditions of the experiments in the previous studies are shown in Table S4.

Table 3. Parameters of the models applied to the results of the equilibrium test with methylene blue.

Model	Parameter	Biochar			Hydrochar		
		BW-BC	CPH-BC	RH-BC	BW-HC	CPH-HC	RH-HC
Langmuir	Q_{max} (mg/g)	243.4	13.6	43.2	20.4	9.5	11.7
	K_L (L/g)	2.296	1.245	1.647	0.417	0.805	0.466
	R^2	0.973	0.832	0.801	0.994	0.965	0.984
	X^2	79.780	3.026	55.998	0.454	0.685	0.451
Freundlich	K_F (mg/g)/(mg/L)^n	166.5	7.3	21.9	7.1	3.9	3.5
	N	0.090	0.155	0.140	0.272	0.242	0.319
	R^2	0.824	0.762	0.588	0.929	0.826	0.973
	X^2	520.685	4.281	115.894	5.814	3.356	0.788
Dubinin-Radushkevich	$q_{DR}(mg/g)$	258.8	15.1	46.3	23.9	11.1	13.9
	K_{DR} (mol^2/kJ^2)	0.0023	0.0038	0.0034	0.0062	0.0050	0.0065
	E (kJ/mol)	13.87	11.44	12.18	8.97	10.02	8.76
	R^2	0.954	0.865	0.713	0.977	0.900	0.989
	X^2	137.18	2.42	80.72	1.85	1.94	0.31

3.3. Pb adsorption tests

In further Pb adsorption experiments, only biochar derived from banana rachis (BW-BC) was considered because of its best textural properties and MB adsorption capacity.

Figure 5a depicts the kinetic curves for both biochar loads. The equilibrium is reached in both loads; however, in the load of 0.5 g/l, it is reached faster than in the load of 0.3 g/l ~20 min and 90 min, respectively. The setup with the higher biochar load reached higher equilibrium level (higher than 150 mg/g) faster than the one with the lower load (around 100 mg/g) because of the higher amount of adsorption active sites present in the loads.

The parameters of the applied model are shown in Table 4. The Pb kinetic data for both initial biochars loads fit the pseudo-second-order model (R^2 0.968 and 0.996 for loads of 0.3 and 0.5 g/L, respectively).

The main chemical species of Pb at pH less than 7 is Pb(II), which could have interacted with the functional groups on the surface of the biochar. According to the relevant literature, the sorption of Pb(II) ions by the adsorbent occurs by ion exchange forming metal complexes in the sites where the metal ion displaces the proton (H^+) [87]. The pH_{PZC} calculated for the sample BW-BC was 8.8 (Figure S4), and the experiments were conducted with initial pHs lower than 6.5. The total charge of the BW-HC was positive. This is a drawback for Pb(II) adsorption; however, biochars are amphoteric materials, with both positively and negatively charged functional groups (see ATR-FTIR analysis, Figure S3), and are able to adsorb pollutants with positive and negative charges.

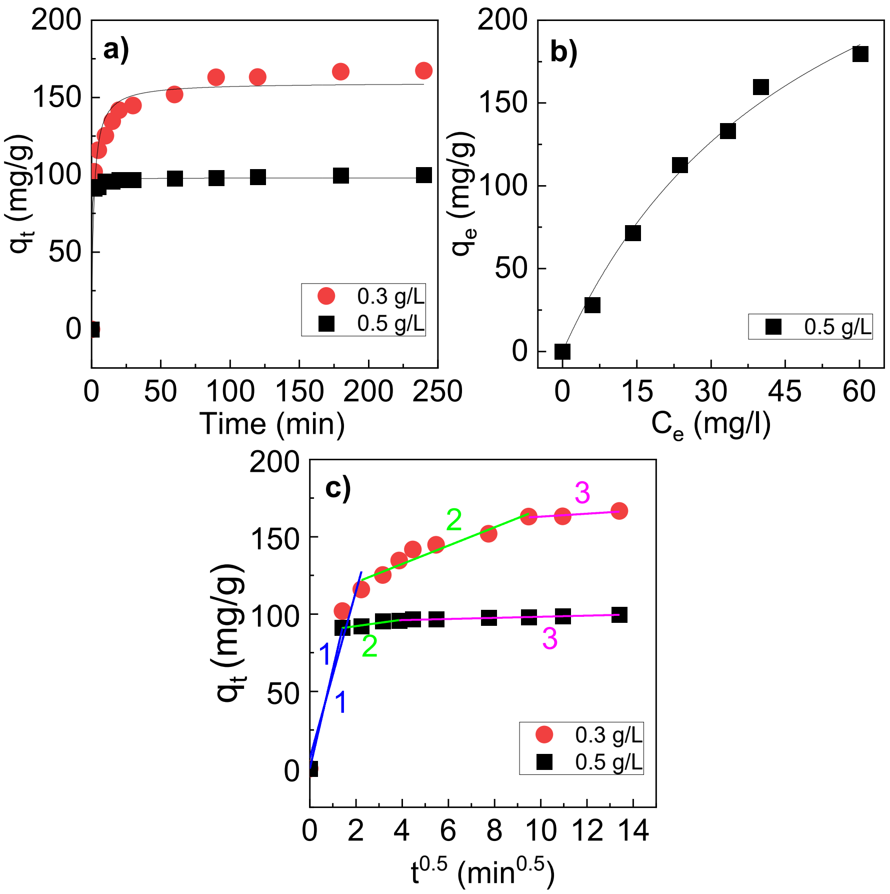

Figure 5. (a) kinetic results and (b) equilibrium adsorption results of Pb(II) of biochar BW-BC. (c) Application of intraparticle model for the kinetic adsorption data: surface diffusion (blue), intraparticle diffusion (green), and adsorption equilibrium (magenta).

For the intraparticle diffusion model, both kinetic data (adsorbent loads of 0.3 and 0.5 g/L) represent the tree sections of the curve (Figure 5c) that correspond to the three stages. However, in the load of 0.5 g/L, the first stage occurred very fast and the difference between the second and third stages is not clearly seen. In the kinetic experiments with an adsorbent load of 0.3 mg/L, the difference between the three stages of the adsorption phenomena can be clearly seen. The parameters of this model are depicted in Table 4. k_{Diff} and C for the adsorbent load 5 g/L showed higher values than those for the load 3 g/L. The higher the adsorbent load, the higher the number of active sites present for adsorption. With an ionic radius of 0.12 nm [87], Pb(II) has a size exclusion limit of 0.2 nm. Thus, the adsorption of Pb(II) to the micropores region within the pore width range of 0-0.2 nm is limited. Intraparticle diffusion (multistep approach) is one of the rate-limiting factors in the adsorption process.

Table 4. Parameters of the models applied to the results of Pb(II) kinetic test of BW-BC.

Models	**Parameter**	**BW-BC**	
		0.3 g/L	**0.5 g/L**
Pseudo-first order	q_1(mg/g)	150.7	97.0
	K_1(min^{-1})	0.420	1.379
	R^2	0.903	0.995
	X^2	227.30	4.43
Pseudo-second order	q_e (mg/g)	159.6	98.0
	K_2(g/mg.min)	0.038	0.054
	R^2	0.968	0.996
	X^2	75.41	1.53
Intraparticle diffusion	k_{Diff1} *(mg/g.min$^{-0.5}$)*	54.001	64.395
	C_1 *(mg/g)*	6.833	1.005
	R_1^2	0.966	1.000
	k_{Diff2} *(mg/g.min$^{-0.5}$)*	5.928	2.078
	C_2 *(mg/g)*	108.701	88.052
	R_2^2	0.960	0.913
	k_{Diff3} *(mg/g.min$^{-0.5}$)*	0.949	0.362
	C_3 *(mg/g)*	153.54	94.642
	R_3^2	0.880	0.960

$^{(*)}$ Data from Elovich is not shown as parameter *a* was excessively high.

The Pb(II) adsorption equilibrium data for BW-BC is shown in Figure 5b. The equilibrium data fit the Dubinin-Radushkevich (R^2= 0.996) and Langmuir models (R^2= 0.992), resulting in a maximum equilibrium concentration of 344.5 mg/g and 270.3 mg/g (Table S5) for the models, respectively. Both values are not consistent since they are clearly outside the values (C_e vs q_e) of the isotherm (Figure 5b). The highest value of q_e reached in the experiments was 179.7 mg/g when the initial Pb(II) concentration was 150 mg/L and the equilibrium concentration (*Ce*) was 60.1 mg/L. This value, 179.7 mg/g, is the highest value of Pb(II) adsorption determined in this study. This value is comparable with those found in the literature for biochars produced from other agricultural wastes, such as rice straw (100-198 mg/g) [88], various biomasses (30-117 mg/g) [89], corn straw (79 mg/g) [90] and hickory (12-17 mg/g) [91]. Further comparison and conditions of the experiments are shown in Table S4.

The value of adsorption energy (*E*), which was calculated using the Dubinin-Radushkevich model, was 4.27 KJ/mol. This value is less than 8 KJ/mol and means that the adsorption process is physical (multilayer). Thus, the Pb(II) adsorption onto BW-BC mainly based on intraparticle diffusion and physical processes.

3.4. Energy storage properties

Biochar from banana rachis was selected to investigate its energy storage properties since it had the best textural properties with S_{BET} higher than 800 m^2/g and better adsorbent capacity. The profiles obtained through CV in 3-electrode cells at 20 mV/s are shown in Figure 6. The figure indicates that the electrochemical profiles obtained in acidic (0.5 M H_2SO_4) and neutral (1 M Na_2SO_4) electrolytes are quasi-rectangular, which correspond to an energy storage mechanism that involves the formation of an electric double-layer at the electrode/electrolyte interphase [92, 93]. In addition to the double-layer mechanism, there is a pair of wide peaks in the voltammogram of the acidic electrolyte (at 0.0/-0.2 V vs SSE), corresponding to redox reactions related to surface oxygen-functional groups in the carbon material [94, 95]. The ATR-FTIR analysis confirmed the presence of oxygen groups, such as C=O, -COOH, C=C, and -C-O. In the neutral electrolyte, a hump on the negative potentials that is related to dihydrogen adsorption on the carbon electrode surface was observed [96]. These semi-rectangular profiles and the peaks related to the oxygen-based functional groups are very common for porous carbon materials, which is consistent with observations in previous studies [48, 97]. Moreover, the voltammogram obtained for the alkaline electrolyte (KOH) showed low current intervals, revealing its detrimental capacitance. Since the calculated pH_{PZC} of BW-BC was 8.8, the charge of the biochar in the alkaline solution (the pH of a 1 M KOH solution is 14) was strongly negative, which prevents electron transfer between the electrolyte and the functional groups of the biochar. Therefore, only 0.5 M H_2SO_4 and 1 M Na_2SO_4 electrolytes were employed for further studies in 2-electrode supercapacitors (SC).

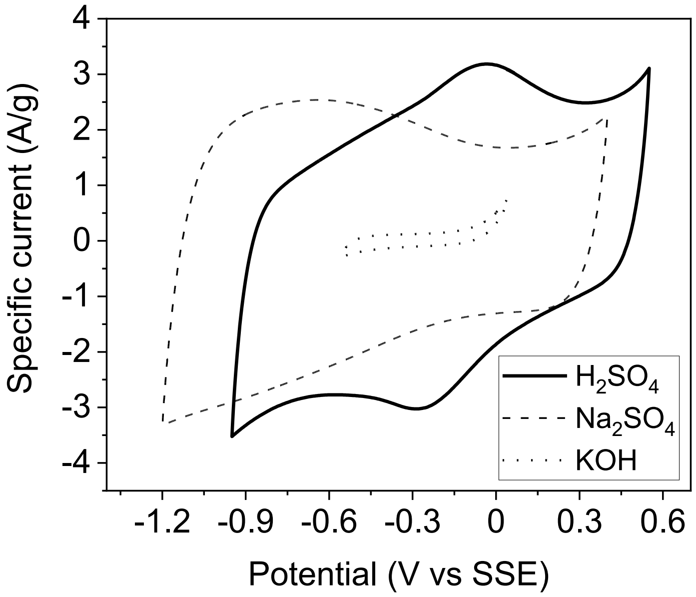

Figure 6. BW-BC voltammograms by using different electrolytes at 20 mV/s.

The assembled asymmetric SC cells were tested using galvanostatic charge/discharge cycling at different specific currents (Figure 7). In both cells, it was possible to appreciate triangular profiles with semi-straight lines, which confirmed that the electric double-layer was the main energy storage mechanism for the BW-BC cells in both electrolytes [98, 99]. The voltage limit for each cell matched the potential window determined previously by CV in 3-electrode cells (Figure 6). The device assembled with the acidic electrolyte (Figure 7a) showed a time-cycle of about 200 s with an applied specific current of 0.25 A/g, which was decreased to ~75 s at 0.50 A/g, ~25 s at 1.00 A/g, ~14 s at 1.50 A/g, and ~8 s at 2.00 A/g. However, the SC assembled with neutral electrolyte (Figure 7b) worked best at a higher voltage (1.6 V), and longer time-cycles were obtained (example ~325 s at 0.25 A/g). In addition, the time-cycle decreased as the specific currents increased (~138 s at 0.50 A/g, ~52 s at 1.00 A/g, ~26 s at 1.50 A/g, and ~15 s at 2.00 A/g). The importance of these analyses is that a longer charge/discharge time at the same specific current indicated greater energy storage properties for the cell with the neutral electrolyte [47].

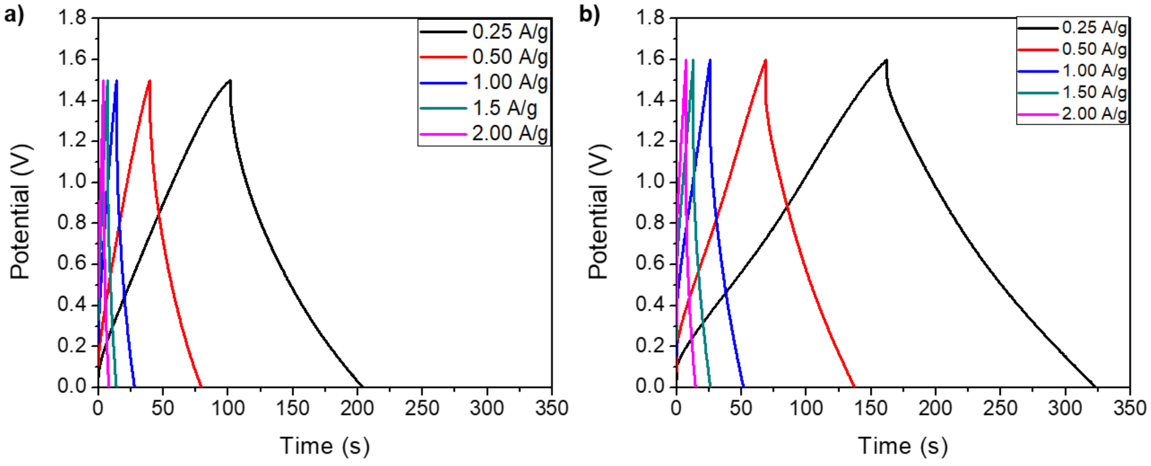

Figure 7. Galvanostatic charge/discharge cycle profiles of supercapacitors cells evaluated in (a) 0.5 M H_2SO_4 electrolyte and (b) 1 M Na_2SO_4 neutral electrolyte

In the stability test, 5000 charge/discharge cycles were performed and modified with applied current every 1000 cycles, using 0.25 A/g (for cycles 1-1000 and 4001-5000), 0.50 A/g (for cycles 1001-2000 and 3001-4000), and 1.00 A/g (for cycles 2001-3000). During the stability test, the capacitance (Figures 8a, b) and the Coulombic and energy efficiencies (Figures 8c, d) were monitored. The capacitance in both SC devices showed the same trend, exhibited the highest capacitance values at 0.25 A/g, and decreased as the specific currents were increased. The above occurred because of an increase in ohmic resistance and a shorter time for the ions in the electrolyte to form a double layer at the electrode/electrolyte interphase [100, 101].

The cell assembled with 0.5 M H_2SO_4 (Figure 8a) exhibited an initial capacitance of 22.2 F/g during the first charge/discharge cycle, which decreased to 16.62 F/g at 0.50 A/g (cycle 1001), then further decreased to 12.77 F/g at 1.00 A/g (cycle 2001), and increased to 17.05 F/g at the end of the cycling at 0.25 A/g, which gave a capacitance retention of 76.8%. However, regarding the device assembled with the neutral electrolyte (Figure 8b) an initial higher capacitance of 28.97 F/g was obtained at 0.25 A/g, which slightly decreased to 25.35 F/g at 0.50 A/g (cycle 1001), then to 22.18 F/g at 1.00 A/g (cycle 2001), and a final value of 24.26 F/g (cycle 5000, 0.25 A/g) was obtained, giving a capacitance retention of 83.7%. The cell with the neutral electrolyte showed better performance based on its capacitance values and capacitance recovery through cycling; this would be further explained. Compared with those of other studies, these supercapacitors exhibit a capacitance retention similar to those previously reported by other researchers [102, 103].

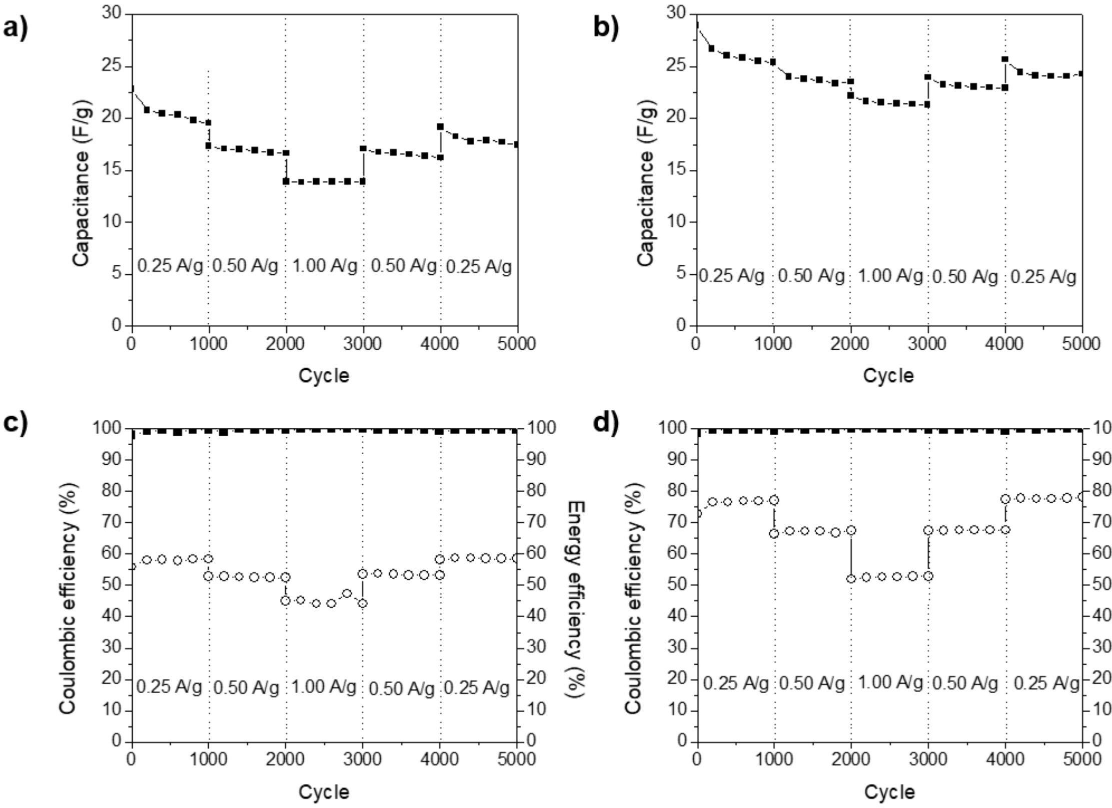

Figure 8. Evolution of capacitance through the cycling of (a) supercapacitor assembled with the acidic electrolyte and (b) supercapacitor assembled with the neutral electrolyte. The Coulombic and energy efficiencies through cycling are shown in (c) supercapacitor in the acidic electrolyte and (d) the neutral electrolyte.

The Coulombic efficiency of both devices (the relationship between the time required for charge and discharge) was close to 100% (Figures 8c and d), irrespective of the specific current applied. However, the energy efficiency (ratio between energy received during charge and delivered in the discharge) was lower in the SC because of energy lost in the form of heat and effects of irreversible faradaic processes, as well as decomposition products that block the pores [50]. The device assembled with the 0.5 M H_2SO_4 electrolyte (open circles, Figure 8c) shows an initial energy efficiency of ~55% at 0.25 A/g, while at 0.50 A/g it decreases to ~52% and ~45% at 1.00 A/g. The same trend was observed for the cell assembled with 1 M Na_2SO_4 (Figure 8d), showing ~73% at 0.25 A/g, ~66% at 0.50 A/g, and ~52% at 1.00 A/g. However, the energy efficiency of the SC cell with the neutral electrolyte was higher, showing improved performance than the device with the acidic electrolyte, where oxygen-based functional groups involved in the storage process are probably being consumed by higher H^+ [50, 104]. In addition, it is well known that neutral electrolytes can reach higher potential windows and their functional groups are electrochemically inert, resulting in the higher energy efficiency observed [105].

The Ragone plots are a useful tool to compare the performance of different energy storage devices in terms of their specific energy and power [106]. Figure 9 shows the plots of the 2-electrode cells assembled with acidic and neutral electrolytes using BW-BC. For comparison, two SC assembled with electrodes made of a commercial carbon, YP50F from Kuraray Corp, in both electrolytes are also plotted. YP50F is an activated carbon obtained from coconut shell and treated with steam that is usually employed for energy storage. Figure 9 indicates that the devices that are based on BW-BC have higher specific energy than those based on YP50F. At 0.25 A/g, BW-BC shows 6.66 Wh/kg and 8.52 Wh/kg in acidic and neutral electrolytes, respectively, whereas YP50F shows 3.99 Wh/kg (acidic electrolyte) and 3.17 Wh/kg (neutral electrolyte). Regarding the specific power, again, the cells assembled with BW-BC have better performance than those assembled with commercial carbon. The devices assembled with BW-BC reached up to 1247 W/kg when 0.5 M H_2SO_4 was used and 1009 W/kg with 1 M Na_2SO_4, whereas the SC based on YP50F only reached 639 W/kg and 895 W/kg in both electrolytes, respectively. Similarly, the electrolytes influenced the behavior of the SC assembled with the same carbon material. BW-BC stores more energy but delivers less power in the neutral electrolyte (Figure 9, red line) than in the acidic electrolyte (Figure 9, dark gray line) at 0.25 A/g, 0.50 A/g, and 1.00 A/g. By contrast, at 1.50 A/g and 2.00 A/g, the energy is higher, and the power is lower in the acidic electrolyte. YP50F can store more energy with less power in the acidic electrolyte (Figure 9, blue line) than in the neutral electrolyte (Figure 9, green line) at 0.25 A/g and 0.50 A/g. The above may be due to diverse factors, such as differences in the rate at which the ions penetrate the pores of the carbon materials, the kinetics of pseudocapacitive processes that are present, and the properties of the cations, [H+] and [Na+] [49]. However, no matter the electrolyte used in these instances, BW-BC had higher energy and power than YP50F and therefore, has a better performance than this commercial carbon for SC.

In addition, Table S6 shows that the energy storage of BW-BC (6.66 -8.52 Wh/kg) is comparable to that of other carbonaceous materials from precursors, such as fir sawdust (9.7 Wh/kg) [107], cotton rose wood (9.4 Wh/kg)[108], corn husk (8.45 Wh/kg) [109], *Miscanthus grass* (8 Wh/kg) [102], *Thespesia populnea* seed (7 Wh/kg) [110], citric acid/urea (6 Wh/kg) [111], tomato plant (4.5 Wh/kg) [112] and corn husk (4.4 Wh/kg) [113].

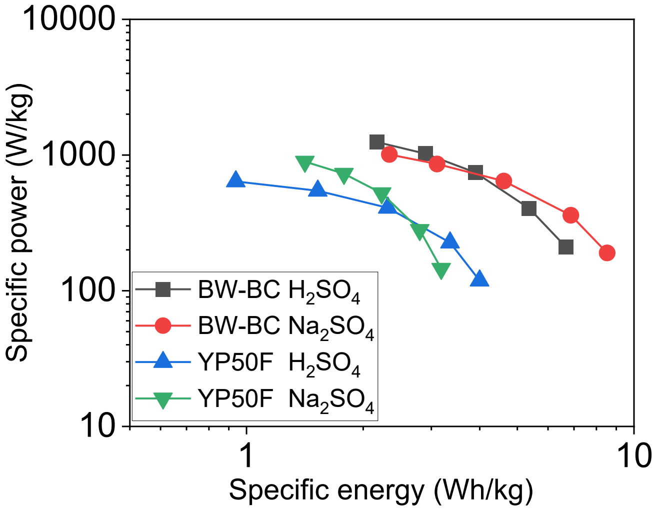

Figure 9. Ragone plots of supercapacitors assembled with BW-BC and the commercial carbon YP50F.

The Nyquist plots of the two supercapacitors assembled with BW-BC are shown in Figure 10a and b. Their profiles correspond to the typical ones observed in supercapacitors where three different regions can be appreciated according to the frequency. At high frequencies, a semicircular loop occurs and denotes a resistive behavior. In the middle-frequencies region, a Warburg diffusion line can be observed; it is in this region where a combination of capacitive and resistive behavior occurs. Finally, at low frequencies, a vertical line appears that indicates a capacitive behavior through the electric double-layer [114, 115]. Through electrochemical impedance spectroscopy (EIS), it is possible to determine the different resistances of the device based on the intercept of the semicircular loop with the real axis and the resistance at low frequencies [116]. The first intercept of the semi-circular loop with the real axis corresponds to electric resistance of all the connections (the resistance to the bulk electrolyte, contact between the carbon, current collector, and measurement connections). As shown in Table 5, the electric resistance of the supercapacitors that work with the 0.5 M H_2SO_4 electrolyte is 0.9 Ω during cycle 1 and slightly decreases to 0.7 Ω at cycle 5000. By contrast, the cell that works with 1 M Na_2SO_4 exhibits a similar original resistance of 1.0 Ω at the first cycle and decreases to 0.9 at the final cycle (5000). As a result of the different electrolytes used in both the assembled cells, there was a noticeable difference in the diameters of the semicircular loop for both devices. This diameter represents the resistance at the electrode/electrolyte interphase. The supercapacitor with the acidic electrolyte had a very low electrode/electrolyte interphase of 0.2 Ω that is stable for the 5000 cycles. By contrast, the device with the neutral electrolyte showed a higher resistance of magnitude 2.2 Ω at cycle 1 and 1.8 Ω at cycle 5000. This difference could be attributed to the higher H^+ in the acidic electrolyte that interacts by Van der Waals forces with the oxygenated functional groups present in the carbon surface. Finally, at low frequencies, the real value of the impedance without the 2 resistances previously mentioned determines the ion diffusion resistance. Diffusion resistance for the device with 0.5 M H_2SO_4 started at 3.4 Ω and decreased to 3.3 Ω at the final cycle. For the device assembled with 1 M Na_2SO_4, its resistance had an initial value of 2.5 Ω and finished at 1.9 Ω.

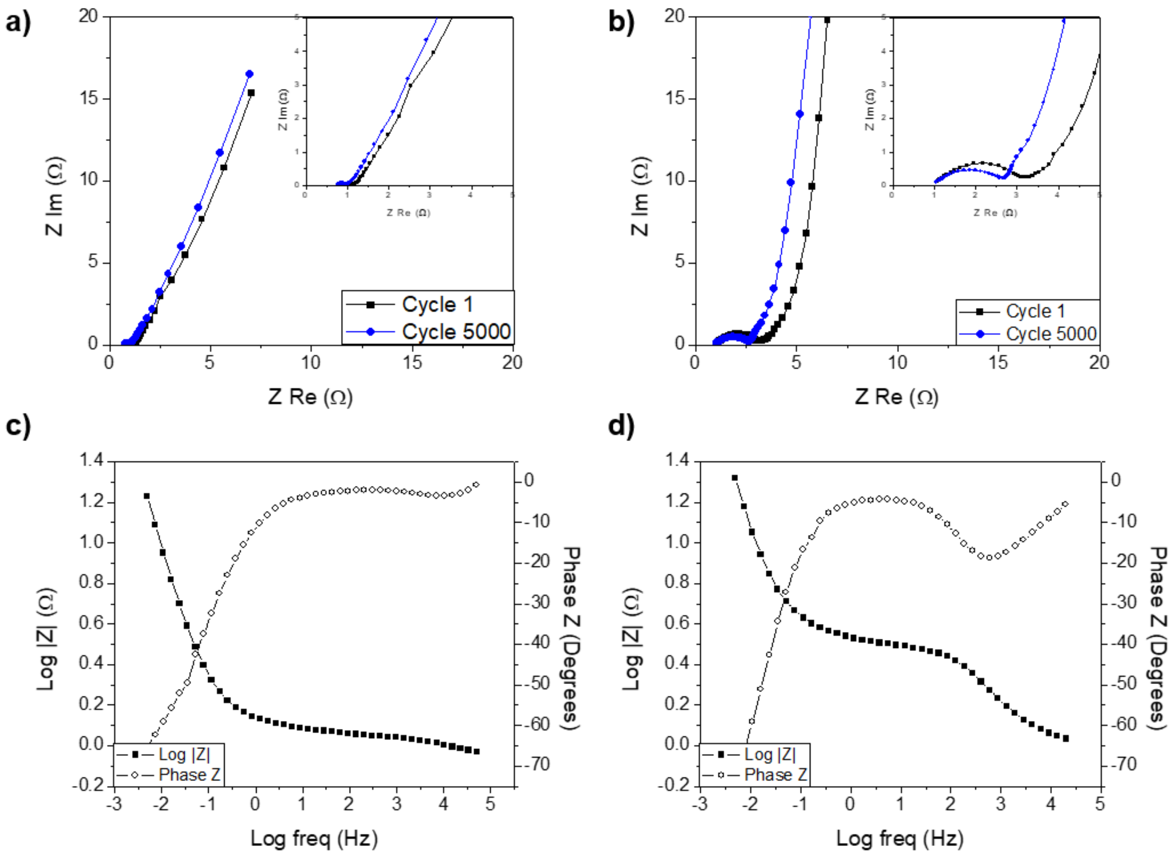

Figure 10. Nyquist plots of the BW-BC supercapacitor using (a) H_2SO_4 electrolyte and (b) Na_2SO_4 electrolyte. Bode plots of the BW-BC supercapacitor using (c) H_2SO_4 electrolyte and (d) Na_2SO_4 electrolyte.

Table 5. Supercapacitor properties of BW-BC determined through electrochemical impedance spectroscopy

SC	**Cycle**	**Phase angle (°)**	**Characteristic frequency (Hz)**	**Relaxation time (s)**	**Electric resistance (Ω)**	**Resistance at interphase (Ω)**	**Diffusion resistance (Ω)**
BW-BC	1	-33	0.037	27.0	0.9	0.2	3.4
H_2SO_4	5000	-38	0.041	24.3	0.7	0.2	3.3
BW-BC	1	-40	0.062	16.2	1.0	2.2	2.5
Na_2SO_4	5000	-42	0.074	13.5	0.9	1.8	1.9

The EIS correlates the logarithm of frequency with the logarithm of the magnitude of the impedance and the phase angle to obtain the Bode plots (Figure 10c and d). In these plots, it is possible to observe an intersection between the lines that represent the magnitude of the impedance and phase angle. The frequency where this intersection occurs is known as the characteristic frequency and corresponds to an angle of -45° for an ideal double-layer capacitor. In both electrolytes, the phase angle became closer to that value after the 5000 charge/discharge cycles can, perhaps, be attributed to the degradation of functional groups that propitiate redox reactions. The device with acidic electrolyte started with a phase angle of -33° and finished at an angle of -38°, and the device with neutral electrolyte had an initial phase angle of -40° and a final angle of -42° (Table 5).

Another change that occurred after the 5000 cycles was that the characteristic frequency became higher. Starting from 0.037 Hz and finishing at 0.041 Hz for the device with the acidic electrolyte and from 0.062 to 0.074 Hz for the cell with the neutral electrolyte. The inverse of this frequency represents the time needed to fully discharge the device with an energy efficiency greater than 50% and is known as the relaxation time. Due to the degradation of the surface functional groups, the time for both supercapacitor devices was shorter, changing from 27.0 to 24.3 s for the cell with the acidic electrolyte and from 16.2 to 13.5 s for the cell with the neutral electrolyte.

4. Conclusion

Biochars and hydrochar with different properties were obtained from agrowastes banana rachis, cocoa pod husk and rice husk at mild conditions. In general, biochars show better properties and methylene blue adsorption capacity than hydrochars. Among the evaluated hydrochar and biochars, biochar derived from banana rachis (BW-BC) has the highest specific surface area (S_{BET}>800m^2/g) and methylene blue adsorption capacity. Additional analyses demonstrate that BW-BC is able to adsorb Pb(II) in a level comparable to the capacity of biochars obtained from other agricultural residues. In the electrochemical studies, BW-BC supercapacitor surpasses the performance of commercial activated carbon YP50F and other carbonaceous materials. The supercapacitor cells assembled with BW-BC/1 M Na_2SO_4 electrode/electrolyte interface presents greater energy storage over the cells with the acidic electrolyte (0.5 M H_2SO_4). The biochar prepared from banana rachis showed the best properties, being potentially useful as adsorbent or as an electrode material for energy storage.

Acknowledgement

The authors would like to thank Universidad Nacional de Tumbes (CANON Projects) and Peruvian National Council for Science and Technology (CONCYTEC) (Contract N° 024-2016-FONDECYT and Contract N ° 160-2018-FONDECYT) for financial support of this project. The Institute of Environmental Technology – Excellent Research (No. CZ.02.1.01/0.0/0.0/16_019/ 0000853) and the ESF in “Science without borders” project, reg. nr. CZ.02.2.69/0.0/0.0/16_027/0008463 within the Operational Program Research, Development and Education were thanked. D.R. Lobato-Peralta would like to thank the National Council of Science and Technology (CONACYT) for the grant for his Ph.D. studies and the projects IG10027 PAPIIT-DGAPA and 279953 from CONACYT. Thanks to Eber Herrera who participated in the experimental work.

References

[1] G. Salmoral, K. Khatun, F. Llive, C.M. Lopez, Agricultural development in Ecuador: A compromise between water and food security?, Journal of Cleaner Production 202 (2018) 779-791.

[2] F. Lu, J. Rodriguez-Garcia, I.V. Damme, N.J. Westwood, L. Shaw, J.S. Robinson, G. Warren, A. Chatzifragkou, S.M. Mason, L. Gomez, L. Faas, K. Balcombe, C. Srinivasan, F. Picchioni, P. Hadley, D. Charalampopoulos, Valorisation strategies for cocoa pod husk and its fractions, Current Opinion in Green and Sustainable Chemistry 14 (2018) 80–88.

[3] R. Campos-Vega, K.H. Nieto-Figueroa, B.D. Oomah, Cocoa (Theobroma cacao L.) pod husk: Renewable source of bioactive compounds, Trends in Food Science & Technology 81 (2018) 172–184.

[4] S. Bhushan, M.S. Rana, Mamta, N. Nandan, S.K. Prajapati, Energy harnessing from banana plant wastes: A review, Bioresource Technology Reports 7 (2019) 100212.

[5] K.A. Adsal, F.G. ÜÇTuĞ, O.A. Arikan, Environmental Life Cycle Assessment of Utilizing Stem Waste for Banana Production in Greenhouses in Turkey, Sustainable Production and Consumption (2020).

[6] M. Adjin-Tetteh, N. Asiedu, D. Dodoo-Arhin, A. Karam, P.N. Amaniampong, Thermochemical conversion and characterization of cocoa pod husks a potential agricultural waste from Ghana, Industrial Crops and Products 119 (2018) 304-312.

[7] G. Cruz, D. Mondal, J. Rimaycuna, K. Soukup, M. Gomez, J. Solis, J. Lang, Agrowaste derived biochars impregnated with ZnO for removal of arsenic and lead in water, Journal of Environmental Chemical Engineering (2020) 103800.

[8] R.K. Srivastava, N.P. Shetti, K.R. Reddy, T.M. Aminabhavi, Sustainable energy from waste organic matters via efficient microbial processes, Sci Total Environ 722 (2020) 137927.

[9] K. Ullah, V. Kumar Sharma, S. Dhingra, G. Braccio, M. Ahmad, S. Sofia, Assessing the lignocellulosic biomass resources potential in developing countries: A critical review, Renewable and Sustainable Energy Reviews 51 (2015) 682-698.

[10] Q. Ma, Y. Yu, M. Sindoro, A.G. Fane, R. Wang, H. Zhang, Carbon-based functional materials derived from waste for water remediation and energy storage, Advanced Materials 29 (2017) 1605361.

[11] O.M. Rodriguez-Narvaez, J.M. Peralta-Hernandez, A. Goonetilleke, E.R. Bandala, Biochar-supported nanomaterials for environmental applications, Journal of Industrial and Engineering Chemistry 78 (2019) 21-33.

[12] J.H. Kwak, M.S. Islam, S. Wang, S.A. Messele, M.A. Naeth, M.G. El-Din, S.X. Chang, Biochar properties and lead(II) adsorption capacity depend on feedstock type, pyrolysis temperature, and steam activation, Chemosphere 231 (2019) 393-404.

[13] V. Turan, Potential of pistachio shell biochar and dicalcium phosphate combination to reduce Pb speciation in spinach, improved soil enzymatic activities, plant nutritional quality, and antioxidant defense system, Chemosphere 245 (2020) 125611.

[14] M.A. Khan, R. Mahmood Ur, P.M.A. Ramzani, M. Zubair, B. Rasool, M.K. Khan, A. Ahmed, S.A. Khan, V. Turan, M. Iqbal, Associative effects of lignin-derived biochar and arbuscular mycorrhizal fungi applied to soil polluted from Pb-acid batteries effluents on barley grain safety, Sci Total Environ 710 (2020) 136294.

[15] M. Zubair, P.M. Adnan Ramzani, B. Rasool, M.A. Khan, M. ur-Rahman, I. Akhtar, V. Turan, H.M. Tauqeer, M. Farhad, S.A. Khan, J. Iqbal, M. Iqbal, Efficacy of chitosan-coated textile waste biochar applied to Cd-polluted soil for reducing Cd mobility in soil and its distribution in moringa (Moringa oleifera L.), Journal of Environmental Management 284 (2021) 112047.

[16] G.J.F. Cruz, L. Matějová, M. Pirilä, K. Ainassaari, C.A. Canepa, J. Solis, J.F. Cruz, O. Šolcová, R.L. Keiski, A Comparative Study on Activated Carbons Derived from a Broad Range of Agro-industrial Wastes in Removal of Large-Molecular-Size Organic Pollutants in Aqueous Phase, Water, Air, & Soil Pollution 226 (2015).

[17] G.J.F. Cruz, M. Pirilä, L. Matějová, K. Ainassaari, J.L. Solis, R. Fajgar, O. Šolcová, R.L. Keiski, Two Unconventional Precursors to Produce ZnCl2-Based Activated Carbon for Water Treatment Applications, Chemical Engineering & Technology 41 (2018) 1649-1659.

[18] M. Boskabady, N. Marefati, T. Farkhondeh, F. Shakeri, A. Farshbaf, M.H. Boskabady, The effect of environmental lead exposure on human health and the contribution of inflammatory mechanisms, a review, Environment international 120 (2018) 404-420.

[19] J. Cruz, G. Cruz, K. Ainassaari, M. Gómez, J. Solís, R. Keiski, Microporous activation carbon made of sawdust from two forestry species for adsorption of methylene blue and heavy metals in aqueous system–case of real polluted water, Revista Mexicana de Ingeniería Química 17 (2018) 847-861.

[20] M.S. Javed, T. Ma, J. Jurasz, M.Y. Amin, Solar and wind power generation systems with pumped hydro storage: Review and future perspectives, Renewable Energy 148 (2020) 176-192.

[21] T. Guo, Y. Liu, J. Zhao, Y. Zhu, J. Liu, A dynamic wavelet-based robust wind power smoothing approach using hybrid energy storage system, International Journal of Electrical Power & Energy Systems 116 (2020) 105579.

[22] M. Winter, R.J. Brodd, What Are Batteries, Fuel Cells, and Supercapacitors?, Chemical Reviews 104 (2004) 4245-4270.

[23] A.K. Cuentas-Gallegos, D. Pacheco-Catalán, M. Miranda-Hernández, Environmentally friendly supercapacitors, Materials for Sustainable Energy Applications: Conversion, Storage, Transmission, and Consumption (2017) 351.

[24] R. Kötz, M. Carlen, Principles and applications of electrochemical capacitors, Electrochimica acta 45 (2000) 2483-2498.

[25] M. Kah, G. Sigmund, F. Xiao, T. Hofmann, Sorption of ionizable and ionic organic compounds to biochar, activated carbon and other carbonaceous materials, Water Res 124 (2017) 673-692.

[26] D. Akhil, D. Lakshmi, A. Kartik, D.-V.N. Vo, J. Arun, K.P. Gopinath, Production, characterization, activation and environmental applications of engineered biochar: a review, Environmental Chemistry Letters (2021).

[27] A. Tomczyk, Z. Sokołowska, P. Boguta, Biomass type effect on biochar surface characteristic and adsorption capacity relative to silver and copper, Fuel 278 (2020) 118168.

[28] R. Gurav, S.K. Bhatia, T.-R. Choi, Y.-L. Park, J.Y. Park, Y.-H. Han, G. Vyavahare, J. Jadhav, H.-S. Song, P. Yang, J.-J. Yoon, A. Bhatnagar, Y.-K. Choi, Y.-H. Yang, Treatment of furazolidone contaminated water using banana pseudostem biochar engineered with facile synthesized magnetic nanocomposites, Bioresource Technology 297 (2020) 122472.

[29] Q. Cao, Z. Huang, S. Liu, Y. Wu, Potential of Punica granatum biochar to adsorb Cu(II) in soil, Scientific Reports 9 (2019) 11116.

[30] Z. Chen, T. Liu, J. Tang, Z. Zheng, H. Wang, Q. Shao, G. Chen, Z. Li, Y. Chen, J. Zhu, T. Feng, Characteristics and mechanisms of cadmium adsorption from aqueous solution using lotus seedpod-derived biochar at two pyrolytic temperatures, Environmental Science and Pollution Research 25 (2018) 11854-11866.

[31] A.E. Creamer, B. Gao, M. Zhang, Carbon dioxide capture using biochar produced from sugarcane bagasse and hickory wood, Chemical Engineering Journal 249 (2014) 174-179.

[32] Z. Tan, Y. Wang, A. Kasiulienė, C. Huang, P. Ai, Cadmium removal potential by rice straw-derived magnetic biochar, Clean Technologies and Environmental Policy 19 (2017) 761-774.

[33] H. Gong, Z. Tan, L. Zhang, Q. Huang, Preparation of biochar with high absorbability and its nutrient adsorption–desorption behaviour, Science of The Total Environment 694 (2019) 133728.

[34] D. Cheng, H.H. Ngo, W. Guo, S.W. Chang, D.D. Nguyen, X. Zhang, S. Varjani, Y. Liu, Feasibility study on a new pomelo peel derived biochar for tetracycline antibiotics removal in swine wastewater, Science of The Total Environment 720 (2020) 137662.

[35] Y. Jia, S. Shi, J. Liu, S. Su, Q. Liang, X. Zeng, T. Li, Study of the Effect of Pyrolysis Temperature on the Cd2+ Adsorption Characteristics of Biochar, Applied Sciences 8 (2018) 1019.

[36] B.T. Nguyen, J. Lehmann, W.C. Hockaday, S. Joseph, C.A. Masiello, Temperature Sensitivity of Black Carbon Decomposition and Oxidation, Environmental Science & Technology 44 (2010) 3324-3331.

[37] L. Li, C. Jia, X. Zhu, S. Zhang, Utilization of cigarette butt waste as functional carbon precursor for supercapacitors and adsorbents, Journal of Cleaner Production 256 (2020).

[38] B. Liu, R. Shi, R. Chen, C. Wang, K. Zhou, Y. Ren, Z. Zeng, Y. Liu, L. Li, Optimized synthesis of nitrogen-doped carbon with extremely high surface area for adsorption and supercapacitor, Applied Surface Science 538 (2021) 147961.

[39] P. Topka, V. Hejtmánek, G.J.F. Cruz, O. Šolcová, K. Soukup, Activated Carbon from Renewable Material as an Efficient Support for Palladium Oxidation Catalysts, Chemical Engineering & Technology 42 (2019) 851-858.

[40] S. Brunauer, P.H. Emmett, E. Teller, Adsorption of gases in multimolecular layers, Journal of the American chemical society 60 (1938) 309-319.

[41] S. Gregg, K. Sing, Adsorption, surface area and porosity. Academic Press, London, Adsorption, surface area and porosity. 2nd ed. Academic Press, London. (1982) -.

[42] J. De Boer, B. Lippens, B. Linsen, J. Broekhoff, A. Van den Heuvel, T.J. Osinga, The t-curve of multimolecular N_2-adsorption, Journal of Colloid and Interface Science 21 (1966) 405-414.

[43] B. Roberts, A procedure for estimating pore volume and area distributions from sorption isotherms, Journal of Colloid and Interface Science 23 (1967) 266-273.

[44] E.P. Barrett, L.G. Joyner, P.P. Halenda, The determination of pore volume and area distributions in porous substances. I. Computations from nitrogen isotherms, Journal of the American Chemical society 73 (1951) 373-380.

[45] A. Ayala-Cortés, D.R. Lobato-Peralta, C.E. Arreola-Ramos, D.C. Martínez-Casillas, D.E. Pacheco-Catalán, A.K. Cuentas-Gallegos, C.A. Arancibia-Bulnes, H.I. Villafán-Vidales, Exploring the influence of solar pyrolysis operation parameters on characteristics of carbon materials, Journal of Analytical and Applied Pyrolysis 140 (2019) 290-298.

[46] A.K. Cuentas-Gallegos, D. Pacheco-Catalán, M. Miranda-Hernández, Environmentally friendly supercapacitors, Materials for Sustainable Energy Applications: Conversion, Storage, Transmission, and Consumption (2017) 370.

[47] D. Martínez-Casillas, I. Mascorro-Gutiérrez, C. Arreola-Ramos, H. Villafán-Vidales, C. Arancibia-Bulnes, V. Ramos-Sánchez, A. Cuentas-Gallegos, A sustainable approach to produce activated carbons from pecan nutshell waste for environmentally friendly supercapacitors, Carbon 148 (2019) 403-412.

[48] D.R. Lobato-Peralta, J. Vazquez-Samperio, O. Pérez, P. Acevedo-Peña, E. Reguera, A.K. Cuentas-Gallegos, Potassium-ion aqueous supercapattery composed by solar carbon and nickel-zinc prussian blue analogue, Journal of Energy Storage 31 (2020) 101667.

[49] D. Martínez-Casillas, I. Alonso-Lemus, I. Mascorro-Gutiérrez, A. Cuentas-Gallegos, Leather waste-derived biochar with high performance for supercapacitors, Journal of The Electrochemical Society 165 (2018) A2061-A2068.

[50] A. Laheäär, P. Przygocki, Q. Abbas, F. Béguin, Appropriate methods for evaluating the efficiency and capacitive behavior of different types of supercapacitors, Electrochemistry Communications 60 (2015) 21-25.

[51] J. Gong, J. Li, J. Xu, Z. Xiang, L. Mo, Research on cellulose nanocrystals produced from cellulose sources with various polymorphs, RSC advances 7 (2017) 33486-33493.

[52] A. Boukir, S. Fellak, P. Doumenq, Structural characterization of Argania spinosa Moroccan wooden artifacts during natural degradation progress using infrared spectroscopy (ATR-FTIR) and X-Ray diffraction (XRD), Heliyon 5 (2019) e02477.

[53] Y. Hou, G. Huang, J. Li, Q. Yang, S. Huang, J. Cai, Hydrothermal conversion of bamboo shoot shell to biochar: Preliminary studies of adsorption equilibrium and kinetics for rhodamine B removal, Journal of Analytical and Applied Pyrolysis 143 (2019) 104694.

[54] K. Kang, S. Nanda, G. Sun, L. Qiu, Y. Gu, T. Zhang, M. Zhu, R. Sun, Microwave-assisted hydrothermal carbonization of corn stalk for solid biofuel production: Optimization of process parameters and characterization of hydrochar, Energy 186 (2019) 115795.

[55] M. Chen, C. Bao, D. Hu, X. Jin, Q. Huang, Facile and low-cost fabrication of ZnO/biochar nanocomposites from jute fibers for efficient and stable photodegradation of methylene blue dye, Journal of Analytical and Applied Pyrolysis 139 (2019) 319-332.

[56] A. Sadezky, H. Muckenhuber, H. Grothe, R. Niessner, U. Pöschl, Raman microspectroscopy of soot and related carbonaceous materials: Spectral analysis and structural information, Carbon 43 (2005) 1731-1742.

[57] S. Reich, C. Thomsen, Raman spectroscopy of graphite, Philosophical Transactions of the Royal Society London A 362 (2004) 2271–2288.

[58] A.C. Ferrari, D.M. Basko, Raman spectroscopy as a versatile tool for studying the properties of graphene, Nat Nanotechnol 8 (2013) 235-246.

[59] S.S. Nanda, M.J. Kim, K.S. Yeom, S.S.A. An, H. Ju, D.K. Yi, Raman spectrum of graphene with its versatile future perspectives, TrAC Trends in Analytical Chemistry 80 (2016) 125-131.

[60] M. Thommes, K. Kaneko, A.V. Neimark, J.P. Olivier, F. Rodriguez-Reinoso, J. Rouquerol, K.S.W. Sing, Physisorption of gases, with special reference to the evaluation of surface area and pore size distribution (IUPAC Technical Report), Pure and Applied Chemistry 87 (2015) 1051-1069.

[61] B. Cagnon, X. Py, A. Guillot, F. Stoeckli, G. Chambat, Contributions of hemicellulose, cellulose and lignin to the mass and the porous properties of chars and steam activated carbons from various lignocellulosic precursors, Bioresource Technology 100 (2009) 292-298.
[62] T.D.M. Florian, N. Villani, M. Aguedo, N. Jacquet, H.G. Thomas, P. Gerin, D. Magali, A. Richel, Chemical composition analysis and structural features of banana rachis lignin extracted by two organosolv methods, Industrial Crops and Products 132 (2019) 269-274.
[63] D. Barana, A. Salanti, M. Orlandi, D.S. Ali, L. Zoia, Biorefinery process for the simultaneous recovery of lignin, hemicelluloses, cellulose nanocrystals and silica from rice husk and Arundo donax, Industrial Crops and Products 86 (2016) 31-39.
[64] M. Prasad, N. Tzortzakis, N. McDaniel, Chemical characterization of biochar and assessment of the nutrient dynamics by means of preliminary plant growth tests, Journal of Environmental Management 216 (2018) 89-95.
[65] N.A.d. Figueredo, L.M.d. Costa, L.C.A. Melo, E.A. Siebeneichlerd, J. Tronto, Characterization of biochars from different sources and evaluation of release of nutrients and contaminants, Revista CiÊncia AgronÔmica 48 (2017).
[66] S. Ali, M. Rizwan, M.B. Shakoor, A. Jilani, R. Anjum, High sorption efficiency for As(III) and As(V) from aqueous solutions using novel almond shell biochar, Chemosphere 243 (2020) 125330.
[67] H. Rajabi, M.H. Mosleh, P. Mandal, A. Lea-Langton, M. Sedighi, Sorption behaviour of xylene isomers on biochar from a range of feedstock, Chemosphere 268 (2021) 129310.
[68] L. Wu, S. Zhang, J. Wang, X. Ding, Phosphorus retention using iron (II/III) modified biochar in saline-alkaline soils: Adsorption, column and field tests, Environmental Pollution 261 (2020) 114223.
[69] M. Wu, X. Han, T. Zhong, M. Yuan, W. Wu, Soil organic carbon content affects the stability of biochar in paddy soil, Agriculture, Ecosystems & Environment 223 (2016) 59-66.
[70] Z. Zeng, S.D. Zhang, T.Q. Li, F.L. Zhao, Z.L. He, H.P. Zhao, X.E. Yang, H.L. Wang, J. Zhao, M.T. Rafiq, Sorption of ammonium and phosphate from aqueous solution by biochar derived from phytoremediation plants, J Zhejiang Univ Sci B 14 (2013) 1152-1161.
[71] H. Wang, C. Fang, Q. Wang, Y. Chu, Y. Song, Y. Chen, X. Xue, Sorption of tetracycline on biochar derived from rice straw and swine manure, RSC Advances 8 (2018) 16260-16268.
[72] Y. Lei, H. Su, F. Tian, A Novel Nitrogen Enriched Hydrochar Adsorbents Derived from Salix Biomass for Cr (VI) Adsorption, Sci Rep 8 (2018) 4040.
[73] J. Chen, L. Zhang, G. Yang, Q. Wang, R. Li, L.A. Lucia, Preparation and Characterization of Activated Carbon from Hydrochar by Phosphoric Acid Activation and its Adsorption Performance in Prehydrolysis Liquor, BioResources 12 (2017).
[74] T. Liu, Y. Guo, N. Peng, Q. Lang, Y. Xia, C. Gai, Z. Liu, Nitrogen transformation among char, tar and gas during pyrolysis of sewage sludge and corresponding hydrochar, Journal of Analytical and Applied Pyrolysis 126 (2017) 298-306.
[75] M. Liang, K. Zhang, P. Lei, B. Wang, C.-M. Shu, B. Li, Fuel properties and combustion kinetics of hydrochar derived from co-hydrothermal carbonization of tobacco residues and graphene oxide, Biomass Conversion and Biorefinery 10 (2019) 189-201.
[76] H. Zhang, F. Zhang, Q. Huang, Highly effective removal of malachite green from aqueous solution by hydrochar derived from phycocyanin-extracted algal bloom residues through hydrothermal carbonization, RSC Advances 7 (2017) 5790-5799.
[77] C. Pelekani, V.L. Snoeyink, Competitive adsorption between atrazine and methylene blue on activated carbon: the importance of pore size distribution, Carbon 38 (2000) 1423-1436.
[78] S. Kasaoka, Y. Sakata, E. Tanaka, R. Naitoh, Design of Molecular Sieving Carbon Studies on Adsorption of Various Dyes in Liquid Phase, NIPPON KAGAKU KAISHI 1987 (1987) 2260-2266.
[79] L. Li, P.A. Quinlivan, D.R.U. Knappe, Effects of activated carbon surface chemistry and pore structure on the adsorption of organic contaminants from aqueous solution, Carbon 40 (2002) 2085-2100.

[80] T. Tatarchuk, M. Myslin, I. Mironyuk, M. Bououdina, A.T. Pędziwiatr, R. Gargula, B.F. Bogacz, P. Kurzydło, Synthesis, morphology, crystallite size and adsorption properties of nanostructured Mg–Zn ferrites with enhanced porous structure, Journal of Alloys and Compounds 819 (2020) 152945.
[81] A.P. Rawat, V. Kumar, D.P. Singh, A combined effect of adsorption and reduction potential of biochar derived from Mentha plant waste on removal of methylene blue dye from aqueous solution, Separation Science and Technology 55 (2019) 907-921.
[82] M.J. Ahmed, P.U. Okoye, E.H. Hummadi, B.H. Hameed, High-performance porous biochar from the pyrolysis of natural and renewable seaweed (Gelidiella acerosa) and its application for the adsorption of methylene blue, Bioresour Technol 278 (2019) 159-164.
[83] M.T. Amin, A.A. Alazba, M. Shafiq, Comparative study for adsorption of methylene blue dye on biochar derived from orange peel and banana biomass in aqueous solutions, Environ Monit Assess 191 (2019) 735.
[84] K.J.L. Dos Santos, G.E.S. Dos Santos, I. de Sa, A.H. Ide, J. Duarte, S.H.V. de Carvalho, J.I. Soletti, L. Meili, Wodyetia bifurcata biochar for methylene blue removal from aqueous matrix, Bioresour Technol 293 (2019) 122093.
[85] B. Ji, J. Wang, H. Song, W. Chen, Removal of methylene blue from aqueous solutions using biochar derived from a fallen leaf by slow pyrolysis: Behavior and mechanism, Journal of Environmental Chemical Engineering 7 (2019).
[86] A.A. Babaei, S.N. Alavi, M. Akbarifar, K. Ahmadi, A. Ramazanpour Esfahani, B. Kakavandi, Experimental and modeling study on adsorption of cationic methylene blue dye onto mesoporous biochars prepared from agrowaste, Desalination and Water Treatment 57 (2016) 27199-27212.
[87] E. Asuquo, A. Martin, P. Nzerem, F. Siperstein, X. Fan, Adsorption of Cd(II) and Pb(II) ions from aqueous solutions using mesoporous activated carbon adsorbent: Equilibrium, kinetics and characterisation studies, Journal of Environmental Chemical Engineering 5 (2017) 679-698.
[88] Z. Shen, D. Hou, F. Jin, J. Shi, X. Fan, D.C.W. Tsang, D.S. Alessi, Effect of production temperature on lead removal mechanisms by rice straw biochars, Sci Total Environ 655 (2019) 751-758.
[89] M.E. Lee, J.H. Park, J.W. Chung, Comparison of the lead and copper adsorption capacities of plant source materials and their biochars, J Environ Manage 236 (2019) 118-124.
[90] Y. Qiao, C. He, C. Zhang, C. Jiang, K. Yi, F. Li, Comparison of Adsorption of Biochar from Agricultural Wastes on Methylene Blue and Pb2+, BioResources 14 (2019) 9766-9780.
[91] Z. Ding, Y. Wan, X. Hu, S. Wang, A.R. Zimmerman, B. Gao, Sorption of lead and methylene blue onto hickory biochars from different pyrolysis temperatures: Importance of physicochemical properties, Journal of Industrial and Engineering Chemistry 37 (2016) 261-267.
[92] P.M. Godwin, Y. Pan, H. Xiao, M.T. Afzal, Progress in Preparation and Application of Modified Biochar for Improving Heavy Metal Ion Removal From Wastewater, Journal of Bioresources and Bioproducts 4 (2019) 31-42.
[93] Q.-Q. Zhuang, J.-P. Cao, X.-Y. Zhao, Y. Wu, Z. Zhou, M. Zhao, Y.-P. Zhao, X.-Y. Wei, Preparation of layered-porous carbon from coal tar pitch narrow fractions by single-solvent extraction for superior cycling stability electric double layer capacitor application, Journal of Colloid and Interface Science 567 (2020) 347-356.
[94] M. Jana, P. Samanta, N.C. Murmu, T. Kuila, Surface modification of reduced graphene oxide through successive ionic layer adsorption and reaction method for redox dominant supercapacitor electrodes, Chemical Engineering Journal 330 (2017) 914-925.
[95] J. Liu, Q. Wang, P. Liu, Redox electroactive group-modified carbon cloth as flexible electrode for high performance solid-state supercapacitors, Colloids and Surfaces A: Physicochemical and Engineering Aspects 588 (2020) 124388.
[96] L. Demarconnay, E. Raymundo-Piñero, F. Béguin, A symmetric carbon/carbon supercapacitor operating at 1.6 V by using a neutral aqueous solution, Electrochemistry Communications 12 (2010) 1275-1278.

[97] D.R. Lobato-Peralta, D.E. Pacheco-Catalán, P.E. Altuzar-Coello, F. Béguin, A. Ayala-Cortés, H.I. Villafán-Vidales, C.A. Arancibia-Bulnes, A.K. Cuentas-Gallegos, Sustainable production of self-activated bio-derived carbons through solar pyrolysis for their use in supercapacitors, Journal of Analytical and Applied Pyrolysis (2020) 104901.
[98] E.A. Arkhipova, A.S. Ivanov, K.I. Maslakov, A.V. Egorov, S.V. Savilov, V.V. Lunin, Mesoporous graphene nanoflakes for high performance supercapacitors with ionic liquid electrolyte, Microporous and Mesoporous Materials 294 (2020) 109851.
[99] Z.-Y. Li, M.S. Akhtar, O.-B. Yang, Supercapacitors with ultrahigh energy density based on mesoporous carbon nanofibers: enhanced double-layer electrochemical properties, Journal of Alloys and Compounds 653 (2015) 212-218.
[100] N. Tisawat, C. Samart, P. Jaiyong, R.A. Bryce, K. Nueangnoraj, N. Chanlek, S. Kongparakul, Enhancement performance of carbon electrode for supercapacitors by quinone derivatives loading via solvent-free method, Applied Surface Science 491 (2019) 784-791.
[101] Y. Zhang, H. Hu, Z. Wang, B. Luo, W. Xing, L. Li, Z. Yan, L. Wang, Boosting the performance of hybrid supercapacitors through redox electrolyte-mediated capacity balancing, Nano Energy 68 (2020) 104226.
[102] G.A. Yakaboylu, C. Jiang, T. Yumak, J.W. Zondlo, J. Wang, E.M. Sabolsky, Engineered hierarchical porous carbons for supercapacitor applications through chemical pretreatment and activation of biomass precursors, Renewable Energy 163 (2021) 276-287.
[103] W. Lu, X. Cao, L. Hao, Y. Zhou, Y. Wang, Activated carbon derived from pitaya peel for supercapacitor applications with high capacitance performance, Materials Letters 264 (2020) 127339.
[104] Y. Li, X. Zhang, J. Deng, X. Yang, J. Wang, Y. Wang, Hierarchical porous biochar derived from cotinus coggygria flower by using a novel composite activator for supercapacitors, Chemical Physics Letters (2020) 137325.
[105] P. Przygocki, Q. Abbas, B. Gorska, F. Béguin, High-energy hybrid electrochemical capacitor operating down to− 40 C with aqueous redox electrolyte based on choline salts, Journal of Power Sources 427 (2019) 283-292.
[106] T. Christen, Ragone plots and discharge efficiency-power relations of electric and thermal energy storage devices, Journal of Energy Storage 27 (2020) 101084.
[107] X. Yang, Q. Wang, J. Lai, Z. Cai, J. Lv, X. Chen, Y. Chen, X. Zheng, B. Huang, G. Lin, Nitrogen-doped activated carbons via melamine-assisted NaOH/KOH/urea aqueous system for high performance supercapacitors, Materials Chemistry and Physics 250 (2020) 123201.
[108] Y. Ma, D. Yao, H. Liang, J. Yin, Y. Xia, K. Zuo, Y.-P. Zeng, Ultra-thick wood biochar monoliths with hierarchically porous structure from cotton rose for electrochemical capacitor electrodes, Electrochimica Acta 352 (2020) 136452.
[109] C.J. Raj, R. Manikandan, M. Rajesh, P. Sivakumar, H. Jung, S.J. Das, B.C. Kim, Cornhusk mesoporous activated carbon electrodes and seawater electrolyte: The sustainable sources for assembling retainable supercapacitor module, Journal of Power Sources 490 (2021) 229518.
[110] K. Manickavasakam, S. Suresh Balaji, S. Kaipannan, A.G. Karthick Raj, S. Veeman, S. Marappan, Electrochemical Performance of Thespesia Populnea Seeds Derived Activated Carbon - Supercapacitor and Its Improved Specific Energy in Redox Additive Electrolytes, Journal of Energy Storage 32 (2020) 101939.
[111] F. Ran, X. Yang, X. Xu, S. Li, Y. Liu, L. Shao, Green activation of sustainable resources to synthesize nitrogen-doped oxygen-riched porous carbon nanosheets towards high-performance supercapacitor, Chemical Engineering Journal 412 (2021) 128673.
[112] D.R. Lobato-Peralta, D.E. Pacheco-Catalán, P.E. Altuzar-Coello, F. Béguin, A. Ayala-Cortés, H.I. Villafán-Vidales, C.A. Arancibia-Bulnes, A.K. Cuentas-Gallegos, Sustainable production of self-activated bio-derived carbons through solar pyrolysis for their use in supercapacitors, Journal of Analytical and Applied Pyrolysis 150 (2020) 104901.

[113] M. Usha Rani, K. Nanaji, T.N. Rao, A.S. Deshpande, Corn husk derived activated carbon with enhanced electrochemical performance for high-voltage supercapacitors, Journal of Power Sources 471 (2020) 228387.
[114] T.N. Phan, M.K. Gong, R. Thangavel, Y.S. Lee, C.H. Ko, Enhanced electrochemical performance for EDLC using ordered mesoporous carbons (CMK-3 and CMK-8): Role of mesopores and mesopore structures, Journal of Alloys and Compounds 780 (2019) 90-97.
[115] C. Jiang, Z. Zou, Waste polyurethane foam filler-derived mesoporous carbons as superior electrode materials for EDLCs and Zn-ion capacitors, Diamond and Related Materials 101 (2020) 107603.
[116] P. Navalpotro, M. Anderson, R. Marcilla, J. Palma, Insights into the energy storage mechanism of hybrid supercapacitors with redox electrolytes by Electrochemical Impedance Spectroscopy, Electrochimica Acta 263 (2018) 110-117.